NAVAL POSTGRADUATE SCHOOL
Monterey, California

AD-A246 203

DTIC
ELECTE
FEB 21 1992
S B D

THESIS

FIBER-OPTIC FLEXURAL DISK ACCELEROMETER

by

Joanne E. Olcott

September 1991

Thesis Advisor: D. A. Brown
Thesis Co-advisor: S. L. Garrett

Approved for public release; distribution is unlimited.

92-03913

92 2 14 059

REPORT DOCUMENTATION PAGE

Form Approved
OMB No. 0704-0188

1a REPORT SECURITY CLASSIFICATION Unclassified	1b RESTRICTIVE MARKINGS
2a SECURITY CLASSIFICATION AUTHORITY	3 DISTRIBUTION / AVAILABILITY OF REPORT Approved for public release; distribution is unlimited.
2b DECLASSIFICATION / DOWNGRADING SCHEDULE	
4 PERFORMING ORGANIZATION REPORT NUMBER(S)	5 MONITORING ORGANIZATION REPORT NUMBER(S)
6a NAME OF PERFORMING ORGANIZATION Naval Postgraduate School 6b OFFICE SYMBOL (If applicable) 3A	7a NAME OF MONITORING ORGANIZATION Naval Postgraduate School
6c ADDRESS (City, State, and ZIP Code) Monterey, CA 93943-5000	7b ADDRESS (City, State, and ZIP Code) Monterey, CA 93943-5000
8a NAME OF FUNDING / SPONSORING ORGANIZATION 8b OFFICE SYMBOL (If applicable)	9 PROCUREMENT INSTRUMENT IDENTIFICATION NUMBER
8c ADDRESS (City, State, and ZIP Code)	10 SOURCE OF FUNDING NUMBERS PROGRAM ELEMENT NO / PROJECT NO / TASK NO / WORK UNIT ACCESSION NO

11 TITLE (Include Security Classification)

FIBER-OPTIC FLEXURAL DISK ACCELEROMETER

12 PERSONAL AUTHOR(S)
Olcott, Joanne E.

13a TYPE OF REPORT	13b TIME COVERED	14 DATE OF REPORT (Year, Month, Day)	15 PAGE COUNT
Master's Thesis	FROM _____ TO _____	1991, September	100

16 SUPPLEMENTARY NOTATION
The views expressed in this thesis are those of the author and do not reflect the official policy or position of the Department of Defense or the U.S. Government.

17 COSATI CODES			18 SUBJECT TERMS (Continue on reverse if necessary and identify by block number)
FIELD	GROUP	SUB-GROUP	Fiber optic, Fiber-optic, Flexural disk accelerometer, Flexural Disk, Accelerometer, Michelson interferometer, Interior Spindle, Acceleration sensitivity

19 ABSTRACT (Continue on reverse if necessary and identify by block number)

The fabrication and calibration of a fiber-optic flexural disk accelerometer is discussed in this thesis. The accelerometer is comprised of a cylindrical body with thin, flexible end plates (or disks) and an interior spindle coupling the disks together ensuring proper phasing. The sensing mechanism is comprised of single mode optical fiber wound into flat coils and epoxied on to the inside faces of the disks, forming the legs of a Michelson interferometer. The use of both legs of this fiber-optic interferometer as sensing elements provides a "push-pull" enhancement and effectively doubles the accelerometer's response while providing common-mode rejection of pressure and temperature variations. The acceleration sensitivity for a sensor consisting of two 1.8" by 1/25" disks is $\Delta\phi/a_c$ = 49 radians/g with a resonance frequency of 2450 Hz. The fractional phase change per unit force is $\Delta\phi/\phi m a_c = 5.5 \times 10^{-9}$ N^{-1}.

20 DISTRIBUTION / AVAILABILITY OF ABSTRACT	21 ABSTRACT SECURITY CLASSIFICATION
☒ UNCLASSIFIED/UNLIMITED ☐ SAME AS RPT ☐ DTIC USERS	Unclassified
22a NAME OF RESPONSIBLE INDIVIDUAL David A. Brown	22b TELEPHONE (Include Area Code) (408) 646-3431 22c OFFICE SYMBOL PH

DD Form 1473, JUN 86 *Previous editions are obsolete* SECURITY CLASSIFICATION OF THIS PAGE
S/N 0102-LF-014-6603 Unclassified

ABSTRACT

The fabrication and calibration of a fiber-optic flexural disk accelerometer is discussed in this thesis. The accelerometer is comprised of a cylindrical body with thin, flexible end plates (or disks) and an interior spindle coupling the disks together ensuring proper phasing. The sensing mechanism is comprised of single mode optical fiber wound into flat coils and epoxied on to the inside faces of the disks, forming the legs of a Michelson interferometer. The use of both legs of this fiber-optic interferometer as sensing elements provides a "push-pull" enhancement and effectively doubles the accelerometer's response while providing common-mode rejection of pressure and temperature variations. The acceleration sensitivity for a sensor consisting of two 1.8" by 1/25" disks is $\Delta\phi/a_c$ = 49 radians/g with a resonance frequency of 2450 Hz. The fractional phase change per unit force is $\Delta\phi/\phi m a_c = 5.5 \times 10^{-6}\ N^{-1}$.

Accession For
NTIS GRA&I ☑
DTIC TAB ☐
Unannounced ☐
Justification
By
Distribution/
Availability Codes
Dist | Avail and/or Special
A-1

III. ACCELEROMETER DESIGN 31

A. INTRODUCTION 31

B. MECHANICAL DESIGN AND DIMENSIONS 31

C. OPTICAL DESIGN 35

D. SENSOR ASSEMBLY PROCESS 39

IV. MECHANICAL TESTING 42

A. RESONANCE FREQUENCY TEST RESULTS 42

1. Motivation 42

2. Tap Test Measurements 42

3. Comparison of the Results to the Handelman and Cohen Theory 51

B. CALIBRATION TESTING 51

1. Instrumentation Set-up 51

a. Piezoelectric 51

b. Optical 55

2. Measurement Technique 55

3. Frequency Response Results and Analysis . . 56

V. CONCLUSIONS AND RECOMMENDATIONS 59

A. PERFORMANCE 59

1. Comparisons to other Fiber-Optic Accelerometers 59

2. Summary 60

B. DESIGN AND OTHER EQUATIONS REVISITED 61

C. RECOMMENDATIONS 62

TABLE OF CONTENTS

I. INTRODUCTION 1

A. BACKGROUND 1

B. FIBER-OPTIC INTERFEROMETERS 1

II. THEORY 4

A. FLEXURAL DISK STRAIN 4

1. Mechanical Theory (Clamped Disk) 4

2. Optical Theory 6

a. Interferometers 6

b. Interferometric Acceleration Sensitivity 9

c. Acceleration Induced Strains 12

B. FLEXURAL DISK WITH ANNULAR CONSTRAINTS 14

1. Introduction 14

2. Annular Disk 18

3. Effects of Adding Mass to a Simple Vibrating System 19

4. Effects of Adding Mass to a Disk 23

C. SIMPLE HARMONIC OSCILLATOR MODEL OF MASS LOADED/MANDRIL STIFFENED DISK 28

1. Lumped Equivalent Parameters 28

2. Resonance Frequency 29

D. DESIGN EQUATION 30

APPENDIX A: COMPONENTS OF THE OPTICAL SYSTEM 64

APPENDIX B: SILVERING OF CLEAVED FIBER ENDS 76

APPENDIX C: TAP TEST DATA 78

LIST OF REFERENCES 82

INITIAL DISTRIBUTION LIST 85

LIST OF TABLES

TABLE 2.1 RESONANCE FREQUENCY FOR A SIMPLY SUPPORTED BOUNDARY CONDITION 18

TABLE 2.2 EIGENVALUES FOR VARIOUS BOUNDARY CONDITIONS (σ = 0.333, RADII RATIO (B/A) = 0.2) 20

TABLE 4.1 SPINDLE AND DISKS COMPOSITE RESONANCE FREQUENCIES FOR VARIOUS COUPLING METHODS 44

TABLE 5.1 COMPARISON OF THREE FIBER-OPTIC ACCELEROMETERS [Ref. 22] 60

LIST OF FIGURES

Figure 2.1 Clamped plate coordinate system [Ref. 1]. . 5

Figure 2.2 Bulk Michelson interferometer [After Halliday and Resnick, Ref. 8]. 6

Figure 2.3 Fiber-optic sensor based on the Michelson interferometer [Ref. 1]. 8

Figure 2.4a Two fiber coil push-pull accelerometer using one disk. 15

Figure 2.4b Two fiber coil push-pull accelerometer using two disks. 15

Figure 2.4c Four fiber coil push-pull accelerometer using two disks. 15

Figure 2.5 Michelson fiber-optic interferometer. . . . 17

Figure 2.5a Two disks, two coils, and a spindle. . . . 17

Figure 2.5b Response of disks, attached fiber coils, and spindle to upward acceleration. 17

Figure 2.6a Addition of primarily mass over a small region to a disk. 21

Figure 2.6b Addition of primarily a stiffening effect by a thin, rigid plate over the entire disk. 21

Figure 2.7a Disk with no added mass. 22

Figure 2.7b Disk with added mass. 22

Figure 2.8a Relationship of the cross-over value, γ_c, (where the loaded resonance frequency crosses over the

unloaded resonance frequency) vs. the radii ratio, $\alpha = a'/a$ [After Handelman and Cohen, Ref. 13]. . . . 26

Figure 2.8b Relationship of the Bessel function, k, and the radii ratio, $\alpha = a'/a$, for various values of the density ratio, $\gamma = \rho' t'/\rho t$ [After Handelman and Cohen, Ref. 13]. 27

Figure 2.9 Two clamped disks with a spindle and a mass loaded double spring harmonic oscillator. 28

Figure 3.1 Cross-sectional view of the accelerometer and spindle dimensions. 32

Figure 3.2 Coupler housing dimensions. 34

Figure 3.3 Winding apparatus [After Brown, Ref. 1]. . . 37

Figure 3.4 Two completed fiber coils before attachment to the body and cap disks. The coupler is visible at the right of the body protruding from the Swageloc™ fitting. 38

Figure 4.1 Block diagram of the free decay experiment apparatus. 43

Figure 4.2 Linear least-square regression analysis for the cap disk. Both the General Radio microphone and Endevco accelerometer data (listed in Appendix C) was used in the analysis. 47

Figure 4.3 Linear least-square regression analysis for the body disk. Both the General Radio microphone and the

Endevco accelerometer data (listed in Appendix C) was used in the analysis. 48
Figure 4.4a Plot of the period squared vs. the added mass for the cap disk. 49
Figure 4.4b Plot of the period squared vs. the added mass for the body disk. 49
Figure 4.5 Block diagram of instrumentation for vibration calibration (solid lines) and optical testing (dashed lines). 52
Figure 4.6 Fiber-optic and piezoelectric accelerometers mounted on the APS Shaker Table. 53
Figure 4.7 Piezoelectric accelerometer signal (lower trace) for 7.3 m/sec^2 peak-to-peak and the interferometric signal showing 6.0 fringes per peak-to-peak excursion at a frequency of 1 kHz. 57
Figure 4.8 Acceleration sensitivity as a function of frequency for this fiber-optic accelerometer. . . . 58
Figure 5.1 Variation of the flexural disk accelerometer [After Brown, Hofler, and Garrett, Ref. 24]. . . . 63

LIST OF SYMBOLS

a = radius of a disk

a_c = acceleration

A = area over which a normal force is applied

b = inner radius of a wound fiber coil

c = outer radius of a wound fiber coil

d = optical path length

D = outer diameter of the optical fiber

E = Young's modulus

f = frequency

f_o = resonance frequency

F = normal force

h = half thickness of a disk

k = optical wave number in a vacuum = $2\pi/\lambda$

k_{eff} = effective stiffness

k_g = optical wave number in glass = $2\pi n/\lambda$

L = length of fiber wound into a single sensing coil

m = mass

m_{eff} = effective mass

M = acceleration sensitivity

M_n = normalized acceleration sensitivity

n = index of refraction of an optical fiber core

P = applied pressure

r = radial location on a disk

t = disk thickness

T = period of oscillation

α = radius ratio of an added mass to a disk radius

$\epsilon_t(r)$ = tangential strain at a radial location r

γ = height ratio of an added mass to a disk thickness

γ_c = cross-over value relating γ to α

λ = wave length of light

Λ = eigenvalue solution to Bessel equation

ϕ = radian path length

ρ = material density

σ = Poisson's ratio

ξ = interferometer configuration parameter

ACKNOWLEDGEMENTS

I would like to thank my advisor, Dr. David Brown, and my co-advisor, Professor Steve Garrett, for their extreme patience as I muddled my way toward the end of this thesis. I would especially like to thank them for answering my many questions and for pointing out alternative solutions to problems encountered during this research. Last but not least for their patience over the past two years as they waited for this thesis to be completed - thank you.

The following individuals also contributed immeasurably to this effort and have my sincerest thank you: Mr. Kupiec (Physics Department University of Alabama), Bob Sanders, and Tom Kellogg (Naval Postgraduate School) for their assistance with the silvering process used to silver the fiber ends; Steve Blankschein and George Jaksha of the Physics Department machine shop for their skilled fabrication of the accelerometer parts; Jay Adeff who would take time out from his own work to answer questions and provide assistance; and last but not least to the other members of IX-81 (from the head boulder to the rest of the pebbles) thanks.

I. INTRODUCTION

A. BACKGROUND

The fiber-optic flexural disk accelerometer discussed in this thesis is one of a series of all-fiber interferometric sensors that have been designed and constructed at the Naval Postgraduate School. This accelerometer is designed to work without a reference fiber in a push-pull configuration. A noteworthy feature of this design is that the optical sensing fibers comprising the push-pull legs of a Michelson interferometer are totally internal to the sensor body. This accelerometer design is based on the "rewiring" of a fiber-optic flexural disk hydrophone that was optimized for sensing acoustic pressures [Ref. 1 - 2]. The fiber-optic flexural disk accelerometer is designed to respond to acceleration and to be insensitive to pressure.

B. FIBER-OPTIC INTERFEROMETERS

Fiber-optic sensors employing interferometric measurement techniques can be considered a subset to one of two general categories used to define sensors that utilize optical fiber. The two categories are intrinsic and extrinsic. In intrinsic devices the light is contained in the optical fiber whereby some means causes a change in either the intensity or phase of the light property in the fiber. In an extrinsic device the

light leaves the optical fiber and interacts with a transducer that responds to the field of interest. The optical fiber interferometric device fabricated in this thesis is of the intrinsic type. A phase difference is created in the legs of the interferometer which is converted in to light intensity modulations at the location of the fiber coupler. The intensity variations are then detected (remotely) with a photodetector.[Ref. 3]

The use of fiber-optic technology in interferometric sensors has many practical applications. Some of these applications, either being employed or tested, are in the fields of acoustic, temperature, acceleration and magnetic sensing. There are many different construction approaches that have been tested in the design of these sensors. Most of the designs have either incorporated the Mach-Zehnder or the Michelson configuration of optical-fibers for sensing. For those who are interested in more information on fiber-optic interferometers, in general, a number of summary articles are available e.g. Busurin, *et al.* [Ref. 4], Giallorenzi, *et al.* [Ref. 5], Lyamshev, *et al.* [Ref. 6], and Jackson [Ref. 7].

In a Mach-Zehnder configuration, the light is split into two optical-fiber legs, by a 2x2 coupler. One leg is generally used as a reference and the other leg is involved in sensing the chosen field, however, both legs can be used as sensor legs in a push-pull configuration. The light is then

recombined at a second 2x2 coupler with an optical-fiber output leg connected to a photodetector.

The Michelson configuration is one in which the light is also split by a 2x2 coupler into two optical-fiber legs. However, instead of recombining the two legs with a second coupler, as the case with the Mach-Zehnder configuration, the ends of the two fiber legs are cleaved, polished, and silvered to enhance reflection of the light (much like a mirror) to the 2x2 coupler where the light was originally split. From the coupler the light is directed into the fiber leg leading to the detection equipment.

II. THEORY

A. FLEXURAL DISK STRAIN

1. Mechanical Theory (Clamped Disk)

A circular clamped disk is defined as a disk for which the strain and vertical displacement are zero at the outer boundary. The strain on one side of the disk at a given location r is equal in magnitude but opposite in sign to the strain developed on the opposite side of the disk at that same radial location. It can be shown that the tangential strain between the top and bottom surfaces of a disk at a radial location r is [Ref. 1]:

$$e_t(r) = \frac{-3P(1-\sigma^2)}{16Eh^2}(a^2-r^2), \qquad (2.1)$$

where P is the applied pressure, E is the Young's modulus, a is the radius of the disk, σ is Poisson's ratio, and h is the half-thickness of the disk as shown in Figure 2.1.

Equation (2.1) defines the differential strain in terms of a uniform pressure (P), in order to evaluate the strains produced by an acceleration of the disk we need the relationship between pressure and acceleration. We can derive this from first principles, by noting first that

$$P = \frac{F}{A}, \qquad (2.2)$$

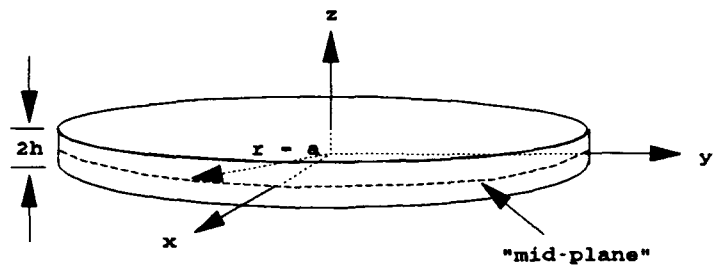

Figure 2.1 Clamped plate coordinate system [Ref. 1].

where F is the normal force and A the area over which it is applied, and from Newton's 2nd Law,

$$F = ma_c, \tag{2.3}$$

where m is mass and a_c is acceleration. The equivalent pressure can then be defined in terms of a normal acceleration as

$$p=\frac{F}{A}=\frac{ma_c}{A}. \tag{2.4}$$

By substituting eqn. (2.4) into eqn. (2.1) the differential strain, as a function of acceleration, a_c, becomes:

$$\epsilon_t(r)=\frac{-3}{16}\left(\frac{ma_c}{A}\right)\frac{(1-\sigma^2)}{16Eh^2}(a^2-r^2). \tag{2.5}$$

2. Optical Theory

a. *Interferometers*

A bulk Michelson interferometer is shown in Figure 2.2 [Ref. 8]. Let light from a source S be incident on a mirror M, which is silvered in such a manner that half of the light is transmitted and half of the light is reflected. The light that is transmitted will strike a silvered mirror M_1 and be reflected back along its incident path. In the same manner the light that was reflected will strike mirror M_2, which will reflect the light back along its incident path.

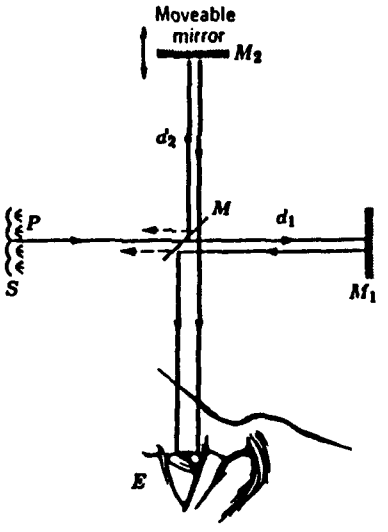

Figure 2.2 Bulk Michelson interferometer [After Halliday and Resnick, Ref. 8].

Assuming that the light is coherent, the returning light from mirrors M_1 and M_2 will recombine (or interfere) when it reaches the splitter/recombiner mirror M. There will be no

relative phase change between the light waves if the distances that they travel after being split (optical path lengths d_1 and d_2) are equal. If the path length d_2 can be changed by the moveable mirror M_2 than the light wave from M_2 will interfere with light from M_1 and a relative phase change will be observable as a change in intensity at the "eye".[Ref. 8] If the relative change in phase between the two paths is equal to an integral number of half wavelengths then there will be destructive interference. Constructive interference results when the change in phase is an integral number of full wavelengths.

When the path length d_2 is varied a "fringe" pattern will be observable. This "fringe" pattern corresponds to changes in the number of wavelengths in the path length. One "fringe" (light-to-light or dark-to-dark pattern) equates to a phase change of one wavelength. Therefore the larger the path length difference the greater the number of "fringes" observed.

Shown in Figure 2.3 [Ref. 1] is a fiber-optic version of the Michelson interferometer. The coherent light source is a laser which injects light into an optical fiber. This optical fiber is spliced to a 2x2 coupler which splits the light equally into two optical fiber interferometer legs. The light will travel through both the reference and the sensing legs, be reflected from the fiber ends and recombined at the

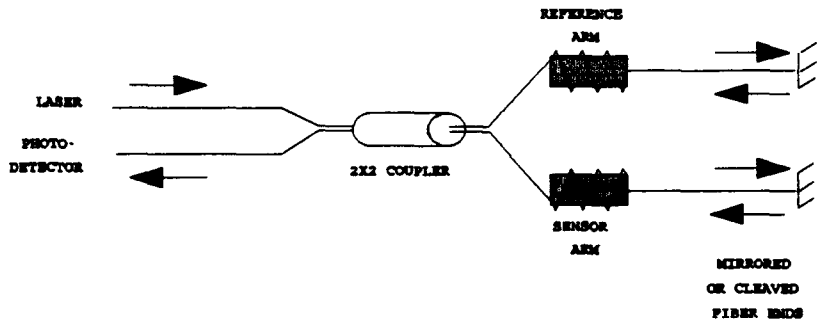

Figure 2.3 Fiber-optic sensor based on the Michelson interferometer [Ref. 1].

coupler. At the coupler the relative phase modulation is converted into an intensity modulation.

If either leg undergoes a relative length change, an intensity change may be seen at the photodetector location. When the lengths of the reference and sensing legs are the same (or differ by an integral number of half wavelengths for the Michelson case) there will be no relative phase change and the output to the photodetector will be constant. This length change can be induced by a variety of different fields such as acceleration, pressure, or temperature. For an accelerometer, the field of interest is the acceleration of the sensor. The phase changes that are induced by the acceleration field may be measured in terms of the number of fringes observed by the photodetector. Each fringe represents one wavelength of (2π radians) of induced phase modulation.

If the reference leg was to be replaced by a second sensing leg, then the observed phase change could be doubled provided that the second sensing leg has an induced length change that is equal in magnitude to the original sensing leg but 180° out-of-phase with respect to it. The resulting "push-pull" effect will create a relative path length difference between the two legs that is twice as large as before. This will produce a relative phase modulation in the interferometer that is twice that of a sensor having only a single sensing leg.

b. Interferometric Acceleration Sensitivity

For a single fiber length, L, the total radian path length is:

$$\phi = knL, \tag{2.6}$$

where $k=2\pi/\lambda$ defines the optical wave number in a vacuum and n is the index of refraction of the core of the optical fiber. Intuitively, ϕ is 2π times the number of wavelengths in glass that will "fit" into a fiber length, L.

Assuming that k, n, and L are functions of only acceleration then the acceleration induced phase change can be found by taking the partial derivative of ϕ with respect to acceleration:

$$\frac{\partial \phi}{\partial a_c} = kn\frac{\partial L}{\partial a_c}\bigg|_{kn} + Lk\frac{\partial n}{\partial a_c}\bigg|_{Lk} + Ln\frac{\partial k}{\partial a_c}\bigg|_{Ln}. \qquad (2.7)$$

For this application, the third term in eqn. (2.7) can be neglected [Ref. 9]. Therefore, eqn. (2.7) can be written:

$$\frac{\Delta \phi}{a_c} = \frac{knL}{a_c}\left[\frac{\Delta L}{L} + \frac{\Delta n}{n}\right]. \qquad (2.8)$$

If k is replaced by $k_g = 2\pi n/\lambda$, the wave number in glass, then eqn. (2.8) can be rewritten to express the phase sensitivity of a Michelson fiber-optic accelerometer giving:

$$M = \frac{\Delta \phi}{a_c} = \frac{\xi k_g L}{a_c}\left[\frac{\Delta L}{L} + \frac{\Delta n}{n}\right]. \qquad (2.9)$$

The extra factor, ξ, in eqn. (2.9), is equal to 2 and arises from the fact that the light will make two passes, in each leg, in a Michelson interferometer, which is the interferometer configuration we choose for this application. Hence eqn. (2.7) and (2.8) (a factor of two not included) would be valid for the more conventional Mach-Zehnder interferometer configuration.

Because the axial strains on the optical fiber arise from the acceleration induced surface strains, the changes in the length of the fiber will have the dominant effect on the sensitivity. The changes in the index of refraction (or the so called photoelastic effects) are neglected in this

derivation, although its magnitude maybe on the order of 20% of the strain induced signal and of opposite sign [Ref. 10]. Hence the low frequency (below resonance) acceleration sensitivity of a fiber-optic clamped flexural disk (Michelson configuration) is:

$$M = \frac{\Delta\phi}{a_c} = \frac{4\pi n}{a_c}\left[\frac{\Delta L}{\lambda}\right]. \qquad (2.10)$$

It is a common practice to consider the normalized sensitivity to allow for easier comparisons between different types of interferometric fiber-optic sensors. This normalization will account for differences in fiber length, laser wavelengths, and the index of refraction. The normalized acceleration sensitivity is found by dividing eqn. (2.10) by the total radian optical path length, $\phi = \xi knL$, of the fiber in a single sensing coil. Thus the choice of Mach-Zehnder or Michelson configuration is independent. It should be noted that ϕ is the radian path length and not the physical length of the fiber. It is the convention, based on historical precedence, that we divide by the length of only one fiber leg even though both legs of a push-pull configured sensor are sensing legs. The normalized acceleration sensitivity is:

$$M_n = \frac{\Delta\phi}{\xi\phi a_c} = \frac{2\xi\pi n}{\xi\phi a_c}\left[\frac{\Delta L}{\lambda}\right] = \frac{\Delta L}{\xi a_c L}. \qquad (2.11)$$

c. Acceleration Induced Strains

The surface strain on a disk can be detected using an all fiber Michelson interferometer. The "push-pull" behavior can be accomplished by winding each leg into to a flat, spiral coil and attaching the coils to either side of a clamped disk. To create an equal but opposite change of length in the sensing legs of the interferometer requires that a "push-pull" mechanism be designed so that a differential strain will be produced. When the disk is accelerated a differential strain equal in magnitude but opposite in sign will be produced on each disk surface (eqn. (2.5)). Assuming that the strain at the surface of the disk is equal to the strain induced in the core of the optical fiber, which is bonded closely to the surface of the disk, the differential fiber strain between the coils on either side of the disk is equal to the differential disk strain predicted by eqn. (2.1). Hence,

$$\frac{\Delta L}{L}(r) = \epsilon_t(r), \tag{2.12}$$

where $\Delta L/L$ represents the relative strain in the interferometer. The total length of optical fiber in a coil of concentric, closely wrapped fiber is given by,

$$L = \int_b^c \frac{2\pi}{D} r dr = \frac{\pi}{D}(c^2-b^2), \tag{2.13}$$

where b and c are the inner and outer radius of the fiber coil and D is the diameter of the fiber. Note that as c goes toward a, the radius of the disk, and b goes to zero the total length of a single layer of fiber is just proportional to the area of the disk, i.e., πa^2. The strain induced path length difference in the interferometer legs is found by substituting eqn. (2.5) into eqn. (2.12) [Ref. 2]:

$$\begin{aligned}\Delta L &= \int_b^c \epsilon_t(r)\,\frac{2\pi}{D}\,r\,dr \\ &= -\frac{3}{16}\left(\frac{ma_c}{A}\right)\left[\frac{(1-\sigma^2)}{Eh^2}\right]\left(\frac{2\pi}{D}\right)\int_b^c (a^2-r^2)\,dr \\ &= -\frac{3}{16}\left(\frac{ma_c}{A}\right)\left[\frac{(1-\sigma^2)}{Eh^2}\right]\left(\frac{2\pi}{D}\right)\left[\frac{a^2}{2}(c^2-b^2) + \frac{1}{4}(b^4-c^4)\right].\end{aligned} \tag{2.14}$$

Equation (2.14) describes the induced path difference between two coils mounted on each side of a single disk as in Figure 2.4a. This equation is also applicable to the case where one fiber coil is mounted to the opposite side of a second disk as in Figure 2.4b (provided that the two disks are of the same dimension, have the same boundary conditions, and have the same phasing). Equation (2.14) also describes the case where there are two fiber coils per sensing leg of the interferometer and they are mounted to two disks as illustrated in Figure 2.4c. Note that in Figures 2.4a-c the optical fiber size has been distorted for illustrative purposes.

If eqn. (2.14) is divided by the total length of fiber in one coil then the acceleration induced fiber strain between the two coils is [Ref. 2]:

$$\frac{\Delta L}{L} = -\frac{3}{32}\left(\frac{ma_c}{A}\right)\left(\frac{1-\sigma^2}{Eh^2}\right)(2a^2-b^2-c^2)\,. \tag{2.15}$$

Note that by convention, we divide by the length of fiber in only one coil. If the fiber is wrapped to the outer edge of the disk (c=a) then eqn. (2.15) will reduce to:

$$\frac{\Delta L}{L} = -\frac{3}{32}\left(\frac{ma_c}{A}\right)\left(\frac{1-\sigma^2}{Eh^2}\right)(a^2-b^2)\,. \tag{2.16}$$

Substituting eqn. (2.15) into eqn. (2.11) will give:

$$M_n = -\frac{3}{32}\left(\frac{m}{\xi A}\right)\left(\frac{1-\sigma^2}{Eh^2}\right)(2a^2-b^2-c^2) \tag{2.17}$$

Equation (2.17) is the normalized sensitivity of a push-pull (two coil) fiber-optic flexural disk accelerometer.

B. FLEXURAL DISK WITH ANNULAR CONSTRAINTS

1. Introduction

In the Flexural Disk Strain section, it was shown that the acceleration induced push-pull performance could be exploited by bonding optical fibers to each side of a clamped disk. The approach taken in this thesis was to use two nominally identical disks with attached fiber coils on the

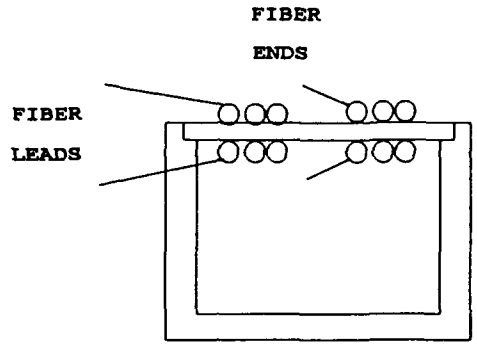

Figure 2.4a Two fiber coil push-pull accelerometer using one disk.

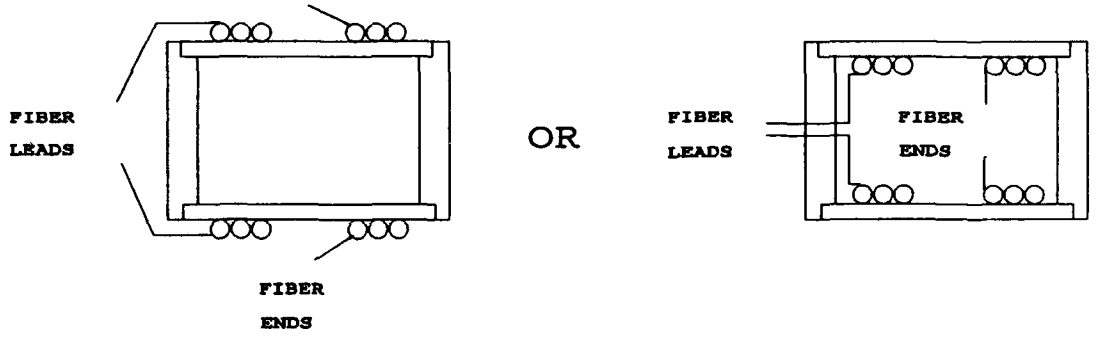

Figure 2.4b Two fiber coil push-pull accelerometer using two disks.

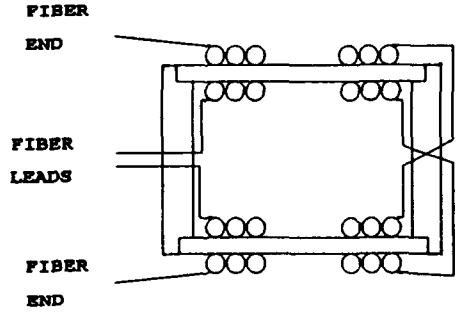

Figure 2.4c Four fiber coil push-pull accelerometer using two disks.

insides of each air backed disk, as depicted in Figure 2.5a. In order to ensure that the disks responded in phase with each other as a single unit, a spindle was designed to fasten the centers of each disk. This permitted only one common degree of freedom. This also reduced the sensor's response to any pressure differential between the inside and outside of the sensor. An illustration of this sensor responding to an upward acceleration can be found in Figure 2.5b.

The purpose of this section is to investigate the behavior of a clamped circular disk that has been modified by means of an attached spindle arrangement. The case of a clamped circular disk with a clamped center will be investigated. An analysis of a loaded clamped disk with concentrically added stiffness and mass will be presented by means of lumped acoustical parameters.

An important design criteria for vibro-acoustic applications is the resonance frequency of the transducer. The resonance frequency will contain information concerning the boundary conditions of the disks and define the upper frequency, in which the sensitivity is independent of frequency. It is advantageous to have a flat frequency response over the region below the disks' resonance frequency.

For the ideally clamped disk, the resonance frequency can be shown to be [Ref. 11]:

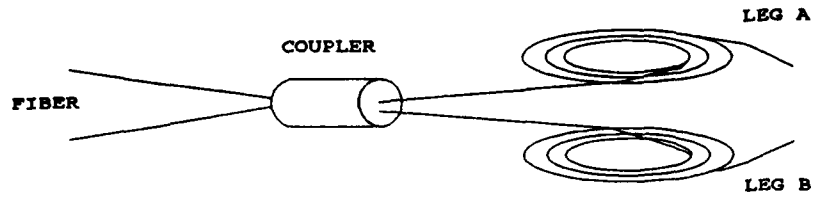

Figure 2.5 Michelson fiber-optic interferometer.

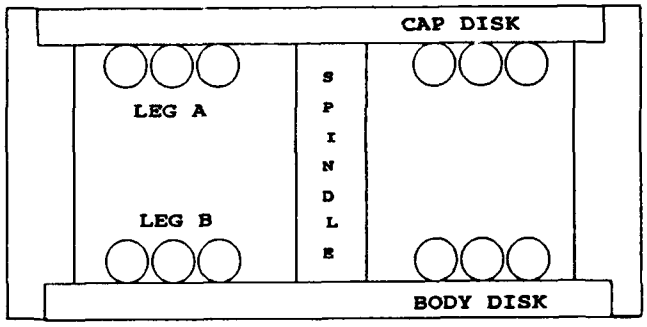

Figure 2.5a Two disks, two coils, and a spindle.

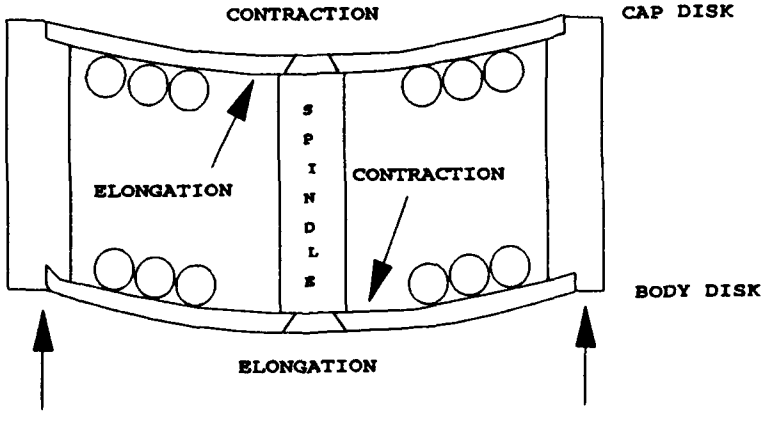

Figure 2.5b Response of disks, attached fiber coils, and spindle to upward acceleration.

$$f_{\bullet} = \frac{\Lambda^2 t}{2\pi a^2}\sqrt{\frac{E}{12\rho(1-\sigma^2)}} \quad . \tag{2.18}$$

In Equation (2.18) Λ is the eigenvalue for the Bessel function solution to the equation of the transverse vibrations of a disk, t is the disk thickness and ρ is the density of the disk material. For a clamped boundary condition Λ is independent of σ and $\Lambda^2 = 10.216$ [Ref. 11 - 12].

If the disk is simply supported at the outer boundary then the resonance frequency, eqn. (2.18), becomes dependent on σ. Various values for Λ, for the fundamental mode of the disk, are listed in Table 2.1 [Ref. 12].

TABLE 2.1 RESONANCE FREQUENCY FOR A SIMPLY SUPPORTED BOUNDARY CONDITION

σ	Λ^2	References
0.250	4.858	[Ref. 11 - 12]
0.300	4.977	[Ref. 11 - 12]
0.333	4.964	[Ref. 11 - 12]

2. Annular Disk

An annular disk is one in which the disk has a concentric circular hole, of radius b, at its center. Since there are now two separate boundary regions to be considered there are an infinite number of boundary conditions that could be considered which span the possibilities between clamped and free. However, there are 3^2 relatively "ideal" boundary conditions for the two regions (i.e., combinations of clamped,

simply supported, and free). A free boundary condition is one in which the edge is not supported in any fashion and it will not be discussed in this thesis. For a given radius, and boundary conditions, the eigenvalue for the Bessel function solution will change depending on the size of the inner hole.[Ref. 12]

Various eigenvalues for the fundamental frequency are listed in Table 2.2 for boundary conditions where the outer boundary is either clamped or simply supported. Tabulated values are for the zero nodal diameter mode only, a Poisson's ratio of 0.333 and a ratio of the inner to outer radii (b/a) of 0.2. Depending on the boundary conditions these eigenvalues will aide in determining the theoretical resonance frequency of an annular disk.[Ref. 12] Measured values for the resonance frequency and comparison to theoretical values are discussed in Chapter IV. From this table it can be seen that for a value of b/a = 0.2, the free-clamped case varies by only 1.21% from the ideal-clamped case.

3. Effects of Adding Mass to a Simple Vibrating System

In the case of a simple vibrating system (or a simple harmonic oscillator), the addition of a rigidly attached mass to the system will effect the resonance frequency. The resonance frequency will either decrease if the addition to the system primarily contributes added mass or the resonance frequency will increase if the contribution is primarily added

stiffness. Figure 2.6a depicts an example of primarily added mass and Figure 2.6b of primarily added stiffness for the addition of a "spindle" to a clamped plate.

TABLE 2.2 EIGENVALUES FOR VARIOUS BOUNDARY CONDITIONS (σ = 0.333, RADII RATIO (B/A) = 0.2)

Inner Boundary	Outer Boundary Clamped	Outer Boundary Simply Supported	Reference
Solid (no inner boundary condition)	10.216	4.977	[Ref. 12]
Free	10.34	4.73	[Ref. 12]
Simply Supported	26.57	17.39	[Ref. 12]
Clamped	36.23	22.79	[Ref. 12]

When the mass added to the system provides both stiffening and mass, then the effect on the unloaded resonance frequency is not as obvious as the two extreme cases. The basic equation for determining resonance frequency of a simple harmonic oscillator is [Ref. 11]:

$$f_n = \frac{1}{2\pi}\sqrt{\frac{k_{eff}}{m_{eff}}} \quad . \tag{2.19}$$

Where k_{eff} represents all of the parameters that provide a stiffening effect to the system and m_{eff} represents all of the parameters that add inertia to the system. By applying eqn. (2.19) to the case of a two dimensional system, such as a flexural disk with added mass, one can attempt to find the

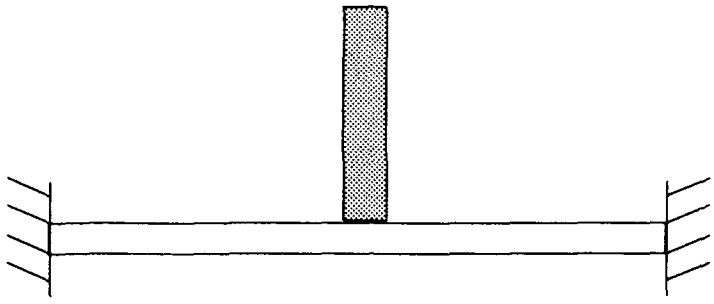

Figure 2.6a Addition of primarily mass over a small region to a disk.

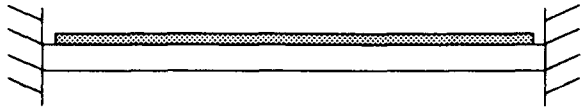

Figure 2.6b Addition of primarily a stiffening effect by a thin, rigid plate over the entire disk.

appropriate effective stiffness and effective mass of the system.

If the disk has a radius, a, and thickness, t (see Figure 2.7a), then the addition of a spindle with radius a′ (a′<a) and thickness t′ (Figure 2.7b) would alter the resonance frequency, eqn. (2.19) by some additional values k′ and m′. The resulting equation for the resonance frequency of this new system is:

$$f_* = \frac{1}{2\pi}\sqrt{\frac{k_{eff} + k'}{m_{eff} + m'}} \quad . \tag{2.20}$$

However, as noted earlier, changes to the resonance frequency are dependent on the relationship between the added mass and stiffness. This relationship is discussed in a paper written in 1956 by George Handelman and Hirsh Cohen [Ref. 13].

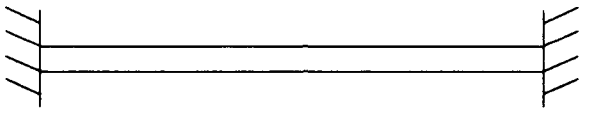

Figure 2.7a Disk with no added mass.

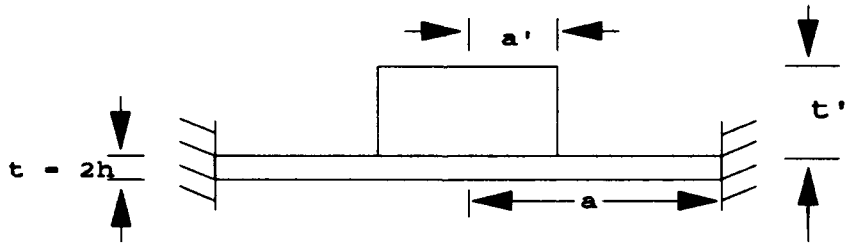

Figure 2.7b Disk with added mass.

4. Effects of Adding Mass to a Disk

If you add both mass and stiffness to a disk, then intuitively you would expect that there would be some combination of the two that would give the same resonance frequency as if there was no additional load on the disk. During a literature search for articles concerning the addition of mass to a disk the paper written by Mr. Handelman and Mr. Cohen was discovered [Ref. 13].

Their paper presents an attempt at quantifying the trade-off between added mass and added stiffness on the resonance frequency of a vibrating system. Their findings indicated that if the ratio between the mass density (ρ) of the disk and the mass density of the disk with added mass (ρ') was less then or equal to one, then the stiffening addition that results from the added mass will always increase the resonance frequency. Figure 2.7b indicates these ratios and relationships. This ratio, γ, is given as:

$$\gamma = \frac{\rho' t'}{\rho t}. \tag{2.21}$$

The ratio of the radius of the added mass to the radius of the disk, α, will also effect the behavior of the resonance frequency. This ratio, α, is given as:

$$\alpha = \frac{a'}{a}. \tag{2.22}$$

Since the added mass (spindle) used in this thesis was milled from the same material as the disks (aluminum), the resulting ratio of the combined mass density and height will reduce to the combined height over the disk's thickness.[Ref. 13]

If the height ratio (γ) is constant, and less than or equal to one, and the ratio of the radii (α) varies, from a' equal to zero to a' equal to a, then the resonance frequency will increase monotonically. If the height ratio is greater than one and the radii ratio is increased from zero to one, the resonance frequency will first decrease, then increase. At some ratio of a' to a the frequency will "cross-over" the resonance frequency of the unloaded plate and will continue to increase.[Ref. 13]

By using the minimum principle in the manner of Rayleigh-Ritz, Handelman and Cohen were able to determine that the lower frequency bound for the value of γ that separates the two resonance frequency behavior regions was roughly γ=2. The point where γ crosses over the value of the resonance frequency of the unloaded disk is termed the cross-over value γ_c. It is at this point where the loaded disk will have the same fundamental frequency as it would if it was unloaded. [Ref. 13]

Figures 2.8a and 2.8b are from the Handelman and Cohen paper and show the results of their calculations [Ref. 13]. In the case of the sensor built in this thesis, the value for

the radii ratio is α = 0.22. It can be seen graphically in Figure 2.8a that the corresponding cross-over value, γ_c, is approximately 2.2. The γ utilized in this system is greater than the value of 2.2 (γ = 9.7) and as a result the resonance frequency will be below the resonance frequency of the unloaded case. Figure 2.8b shows several curves for different values of γ plotted as a function of the radii ratio, α, and the eigenvalue, K, solution to the Bessel functions [Ref. 13].

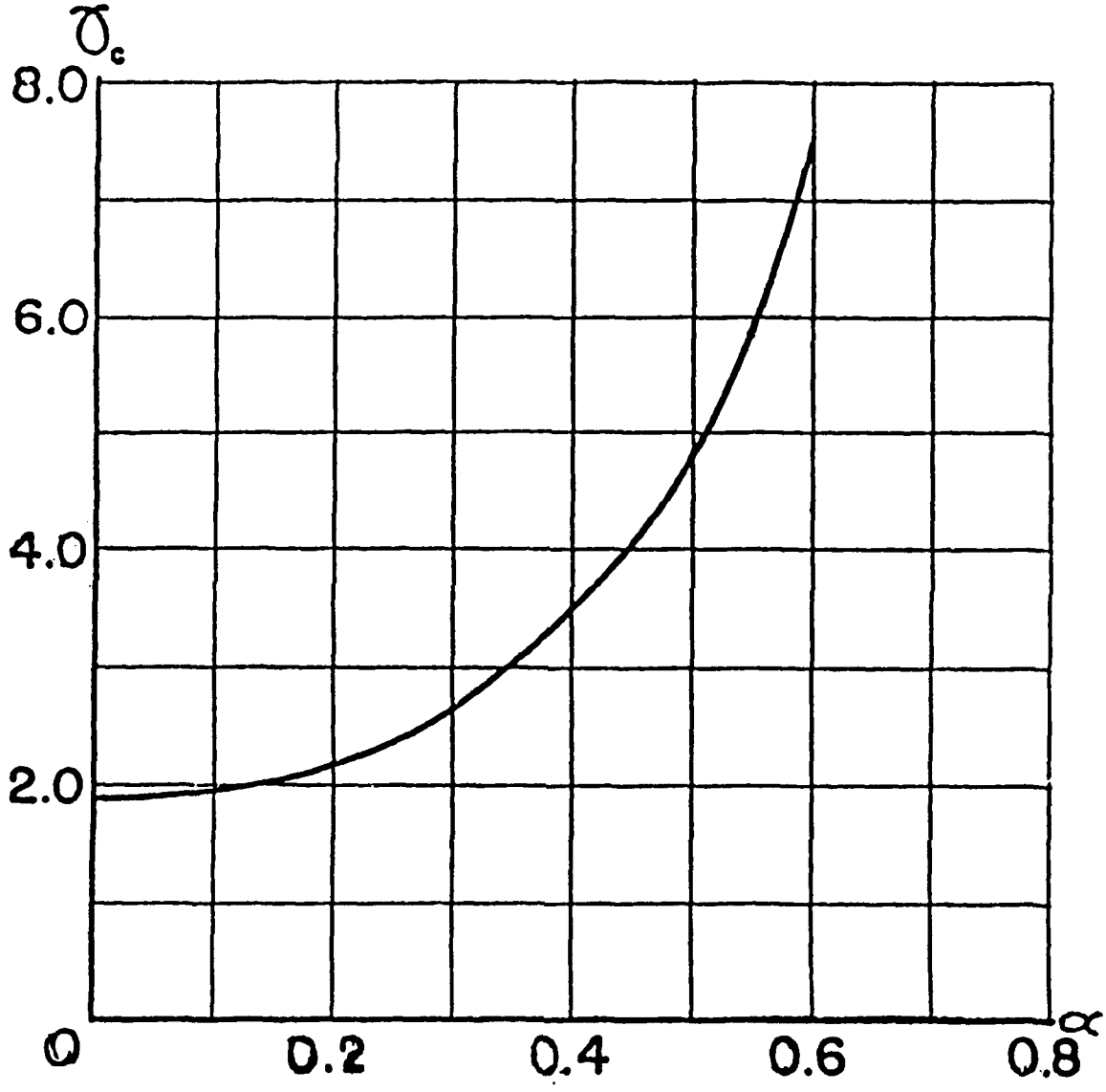

Figure 2.8a Relationship of the cross-over value, γ_c, (where the loaded resonance frequency crosses over the unloaded resonance frequency) vs. the radii ratio, α = a'/a [After Handelman and Cohen, Ref. 13].

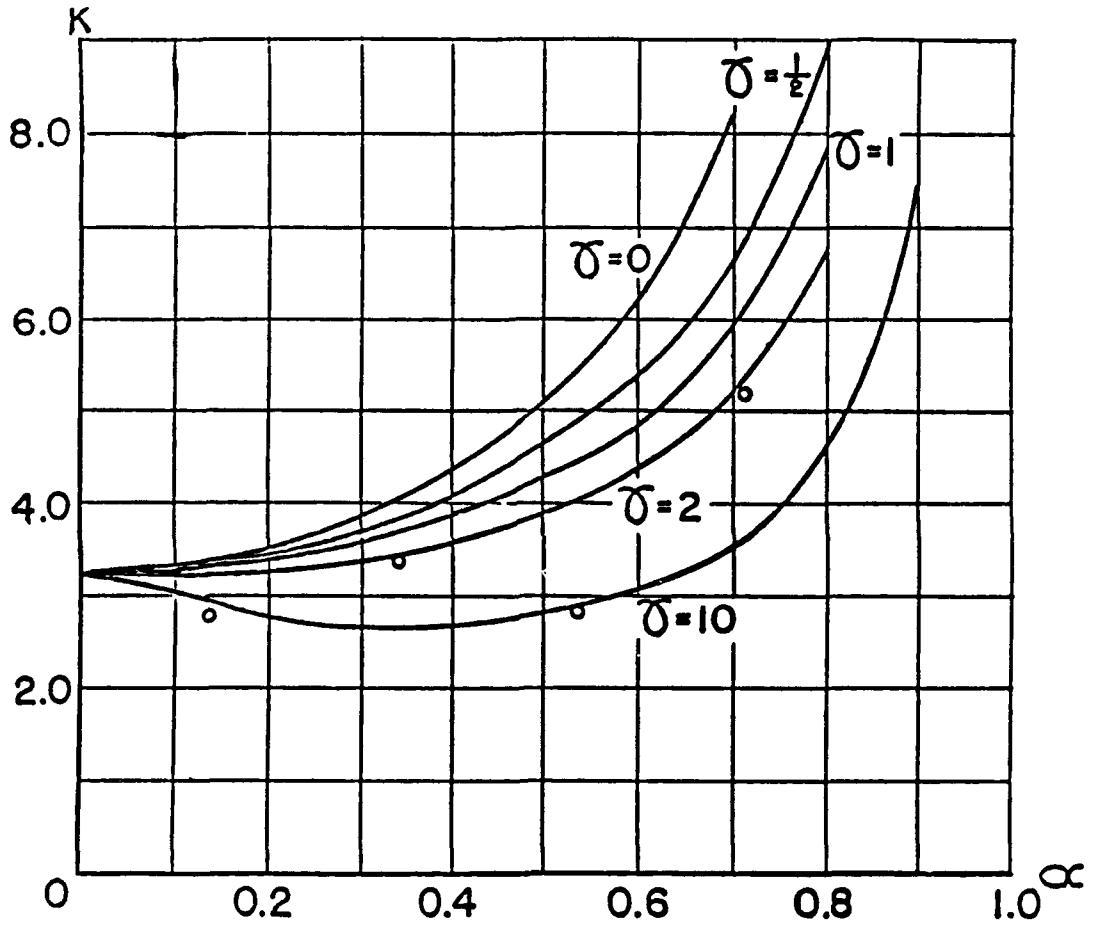

Figure 2.8b Relationship of the Bessel function, k, and the radii ratio, $\alpha = a'/a$, for various values of the density ratio, $\alpha = a'/a$, for various values of the density ratio, $\gamma = \rho' t'/\rho t$ [After Handelman and Cohen, Ref. 13].

C. SIMPLE HARMONIC OSCILLATOR MODEL OF MASS LOADED/MANDRIL STIFFENED DISK

1. Lumped Equivalent Parameters

Another intuitive view of this sensor system comprised of two clamped disks connected by a spindle is to recognize it as mass loaded double spring harmonic oscillator. Figure 2.9 shows these two systems side-by-side. Splitting both diagrams in half (dashed lines) results in a simple harmonic oscillator (single, mass loaded, spring) where the attached mass has half the original mass. Hence the resonance frequency of this accelerometer can be modeled by lumping the effective mass of one of the disks and half of the mass of the spindle together. The effective stiffness of the accelerometer is determined by the stiffness of one of the disks and that stiffness contributed by the spindle.

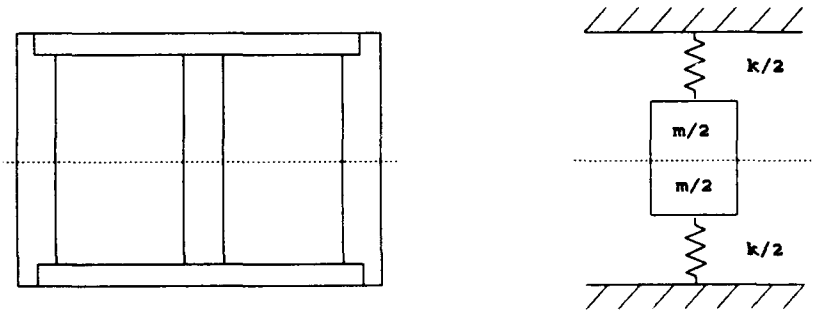

Figure 2.9 Two clamped disks with a spindle and a mass loaded double spring harmonic oscillator.

2. Resonance Frequency

The resonance frequency for the simple harmonic oscillator with a mass of half that of the spindle is given as

$$f_o = \frac{1}{2\pi}\sqrt{\frac{k/2}{m/2}} = \frac{1}{2\pi}\sqrt{\frac{k'}{m'}} \quad . \tag{2.23}$$

This is equivalent to eqn. (2.19) where k′ equals k_{eff} and m′ equals m_{eff}. Equation (2.23) also represents the resonance frequency of a single disk with an attached half-mass.

Expanding this reasoning to cover the case of a double disk (double spring) system with a spindle (mass) coupling the two disks together (as shown in Figure 2.9) results in the resonance frequency being

$$f_o = \frac{1}{2\pi}\sqrt{\frac{k/2+k/2}{m/2+m/2}} = \frac{1}{2\pi}\sqrt{\frac{k}{m}} \quad . \tag{2.24}$$

Equation (2.24) displays the same information as eqn. (2.20). However, there still remains the difficulty of determining what the added stiffness is that is imparted to this system from the attached spindle.

By using the calculations of Handelman and Cohen, and viewing this accelerometer as a double spring, mass loaded harmonic oscillator, it is easier to see that the addition of the spindle should produce the effect of a decrease of the resonance frequency below that of the unloaded system.

D. DESIGN EQUATION

As in any sensor design there will always be some tradeoffs between sensitivity, resonance frequency (bandwidth), and the material used in construction of the sensor. An important design parameter is formed by multiplying the acceleration sensitivity and the square of the resonance frequency. By combining eqn. (2.10), (2.14), and (2.18), and letting a=c and b<<a in eqn. (2.14), and noting that ρ = m/At in eqn. (2.18), we obtain:

$$Mf_{\bullet}^2 = (-0.005)\Lambda^4 t\left(\frac{k_g}{D}\right). \tag{2.25}$$

Where Λ is the appropriate eigenvalue for the Bessel function solution, k_g is the optical wave number in glass, D is the diameter of the optical fiber, and t is the thickness of the disk.

The product of the acceleration sensitivity and the square of the resonance frequency is proportional to the optical wave number in glass, the thickness of the disk, and the inverse of the diameter of the fiber.

III. ACCELEROMETER DESIGN

A. INTRODUCTION

The general design of the Fiber-Optic Flexural Disk Accelerometer is similar to the design of a Flexural Disk Hydrophone discussed in LT. Flayharty and LT. Fitzgerald's thesis [Ref. 2]. The body dimensions of the accelerometer are the same, with changes being made only to the optical wiring scheme in order to provide an optimized response to acceleration with reduced pressure sensitivity, and the addition of an internal spindle to the sensor to ensure that the two disks move in phase.

B. MECHANICAL DESIGN AND DIMENSIONS

The outer diameter of the main cylindrical body housing is 6.0 cm and its height is 2.5 cm. The two disks attached to each end of the housing are nominally 4.6 cm in diameter and 1 mm in thickness. On the inside face of each disk, a flat coil of optical fiber is epoxied (with Stycast® 1266 epoxy) to sense the acceleration induced surface strains in the flexural disks. In addition, a cylindrical aluminum spindle, with diameter 1.0 cm and height of 1.6 cm, is fastened between the two disks by a 10-32 machine screw and nut. The addition of the spindle ensured that the two disks moved together in-phase

for a given acceleration of the sensor body. Figure 3.1 is a cross-sectional view of this accelerometer and spindle.

When an acceleration is applied normal to the disks' surfaces, one disk will deflect inward and the other disk will deflect outward as shown in Figure 2.5b. The coil on the inside face of the cap disk will lengthen while the coil on the inside face of the body disk will shorten. The total change in optical path length of the two fiber interferometer legs will be double that of a single disk and coil. It is this differential behavior that is referred to as a push-pull mode of operation.

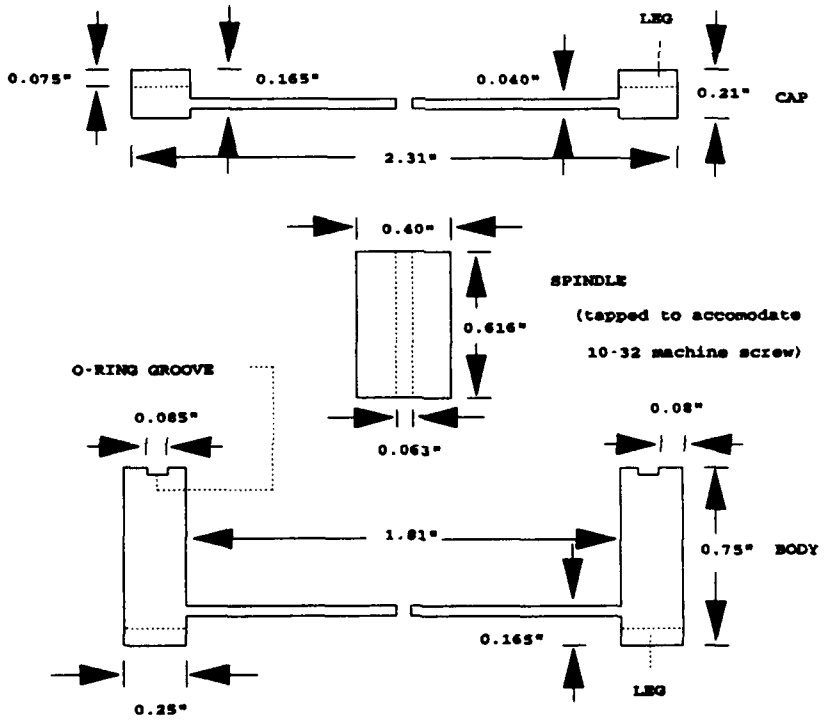

Figure 3.1 Cross-sectional view of the accelerometer and spindle dimensions.

The two sections of the sensor were milled from 6061-T6 aluminum bar stock so that each disk was permanently attached to a section of the cylindrical housing. The body portion of the accelerometer was designed to be the largest piece as it had to accommodate the two Swagelok™ connectors used as access ports. Two threaded holes were fabricated in the housing wall to accommodate the Swageloks™ which were screwed into the wall using Teflon® tape. The 1/4 inch Swagelok™ is used to seal the coupler housing. The 1/8 inch Swagelok™ is used as an evacuation port for creating a vacuum in the sensor as a secondary clamping mechanism.

The groove used to accommodate the O-ring is also machined into the body and was physically located closer to the cap disk than to the body disk. The inclusion of the O-ring allowed for the accelerometer to be made watertight for hydrophone application [Ref. 3]. The O-ring used is a commercially available size (Parker № 2-033).

The flexural disk accelerometer used consisted of the following elements:

1. The main body cylindrical housing including one flexural disk permanently attached. (Body)
2. A second flexural disk. (Cap)
3. An O-ring.
4. A 2x2 fused biconical fiber-optic coupler. The coupler consisted of 10.5 m ± 30 cm long single mode optical fiber (Corning Flexcore™ 850) that make up the sensing legs of the interferometer.

5. Two Swagelok™ fittings, 1/4 inch tube used to hold the coupler, 1/8 inch pipe thread; a 1/8 inch tube that will allow DC calibration by venting the accelerometer, 1/8 inch pipe thread.

6. A coupler housing.

7. Aluminum spindle made of 6061-T6 aluminum bar stock and designed to fit snugly between the two disks. Used to add mass and to insure in-phase motion between the two disks.

Data sheets for the commercially available elements are contained in Appendix A.

The sensor has 1/16 inch bases on the top of the cap and bottom of the cylindrical housing and these can be used as attachment points for clamps should additional clamping be necessary to hold the sensor together. No additional clamping was used in the testing of this accelerometer.

The dimensions of the coupler housing are shown in Figure 3.2. The coupler housing is designed to hold the biconical coupler so that it is not free to either slide in or out of the air-tight sensor body. Additional support was gained by potting the outside end of the coupler housing with Uralite®

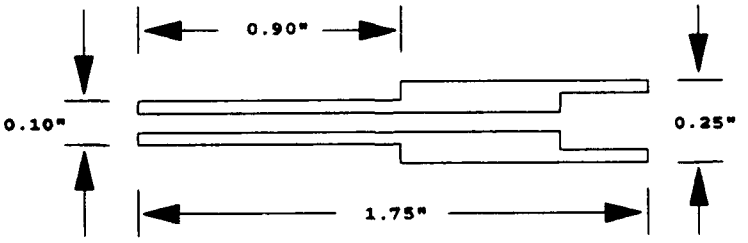

Figure 3.2 Coupler housing dimensions.

3130, an polyurethane casting elastomer. The small diameter portion of the coupler housing will extend only a short way into the interior of the sensor in order to leave room for the spindle.

C. OPTICAL DESIGN

As discussed in Chapter I, this accelerometer uses a fiber-optic Michelson interferometer. An Allied Amphenol 3dB, 2x2 coupler [Ref. 14] is used as the beam splitter in the interferometer. This coupler has four fiber leads, with a nominal split ratio of 50/50 (splits 50% of the input optical power into each fiber leg). One input leg of the coupler is used to inject coherent light from a single mode laser into the coupler which splits the light to two other fiber leads which are themselves the legs of the interferometer. When the light reaches the cleaved or mirrored ends of the legs a percentage of the light will be reflected back through the legs to the coupler. (The portion of the light that exits the cleaved or mirrored end of the fiber is not used in this configuration). The coupler will convert the returned light from a relative phase modulation into an intensity modulation which will propagate down the fourth fiber lead and back to the laser.

The coupler was a custom fabrication since it contained two 10.5 m ± 30 cm long optical fiber leads and two standard 1.0 m ± 23 cm input leads. This enables the interferometer to

be a single unit with no splice joints, which tend to weaken the overall construction of the system, adding significant difficulties in fabrication, as well as creating losses and extra reflections in the light transmitted down and back through the sensing legs. The optical fiber used in the construction of the coupler is Corning Flexcor™ 850, a single mode fiber designed to operate in the 850 nm wavelength region. The core diameter is approximately 8 μm, cladding diameter of 125 μm, and an acrylate coating of 250 μm in diameter [Ref. 15]. The acrylate coated fiber was chosen because of the similarity of its properties to the epoxy that was chosen for bonding the optical fiber to the disks.

Using the apparatus in Figure 3.3 [Ref. 1], flat spiral coils were wound. A flat metal washer, approximately 300 μm thick with an approximate diameter of 1.6 cm, prevents the fiber wraps from slipping past each other and assists in creating a uniformly flat fiber coil with a thickness equal to the diameter of the fiber. In addition, the washer defines the inner diameter of the fiber coil ensuring that the coils would not impinge upon the spindle located between the disks and the fiber would not have an excessively small bend radius which could cause excess light loss.

Care must be taken in winding the fiber around the plates. With only one end free to twist, kinks in the fiber will develop that can lead to the fiber breaking. After one or two

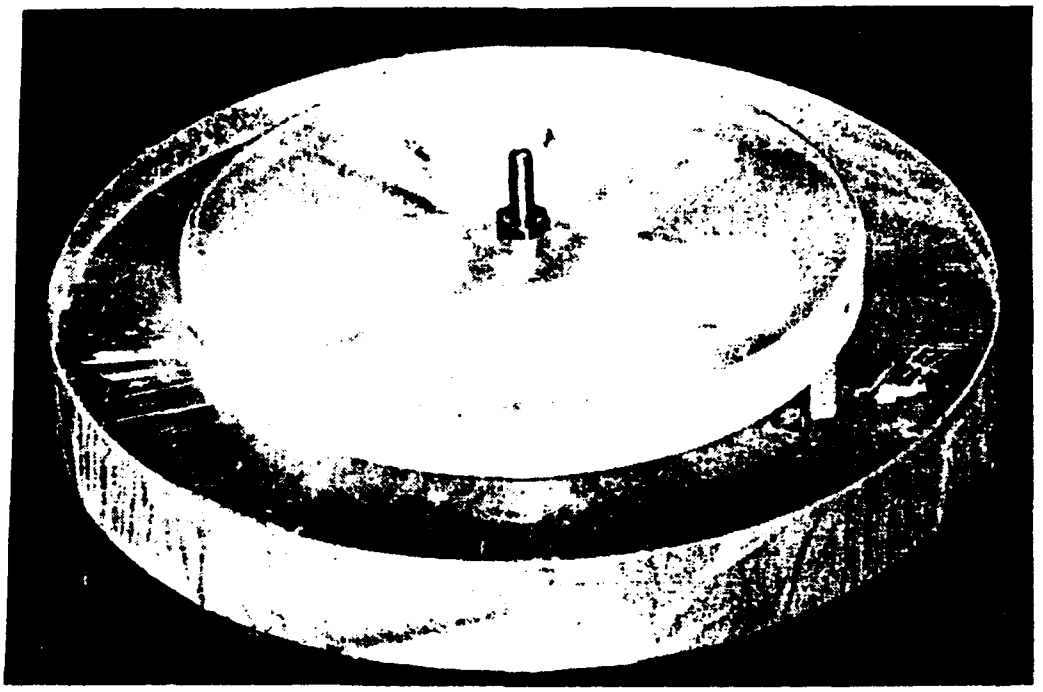

Figure 3.3 Winding apparatus [After Brown, Ref. 1].

passes around the plates the free end of the fiber was allowed to relax (or unkink) to relieve the strain induced in the winding process. The alternative method of winding is to have each end of the fiber free. This allows both ends to twist freely and remain unkinked as the fiber length is coiled.

After the coils were wound they were then taped through the slots of the winding plates. Taping prevents the coils from unwinding when the plates are removed. Once the coils are taken from between the plates, a thin strip of rubber adhesive was applied in all four quadrants. When the adhesive had cured the tape was removed.

Each coil consists of five meters of fiber excluding an additional 20 cm of fiber between the coupler and the start of the coil. This excess amount of fiber allows for positioning of the coil on the disks of the sensor. The inner diameter of each coil is 1.6 cm and the outer diameter is 4.4 cm. Figure 3.4 shows two completed coils.

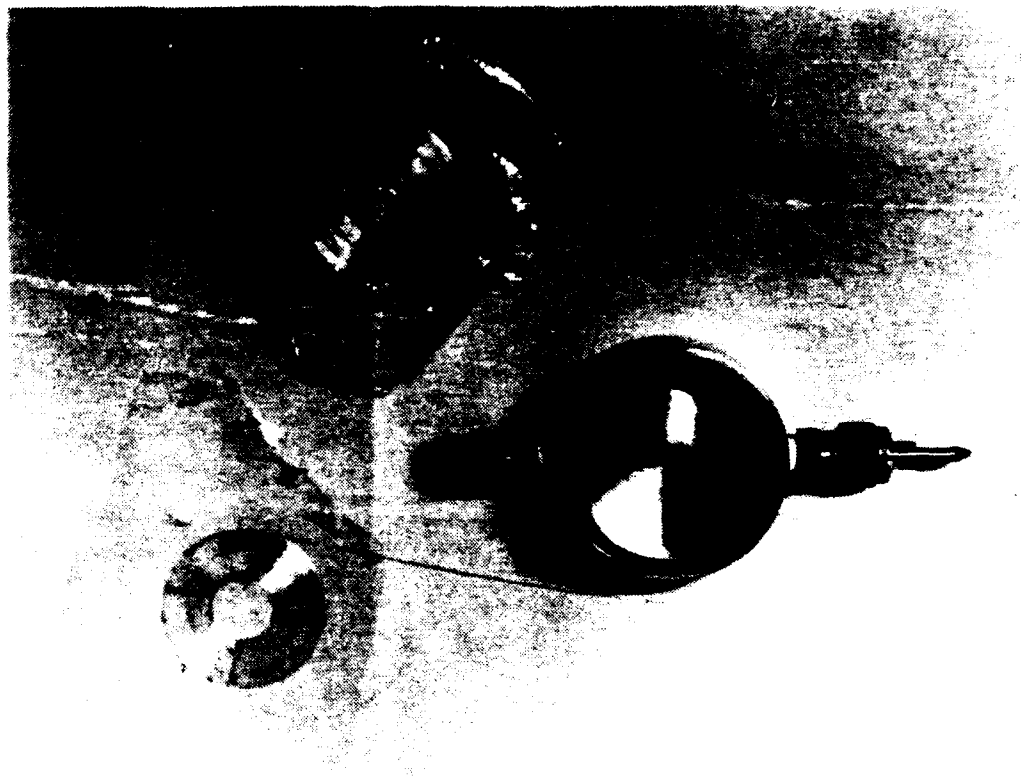

Figure 3.4 Two completed fiber coils before attachment to the body and cap disks. The coupler is visible at the right of the body protruding from the Swageloc™ fitting.

D. SENSOR ASSEMBLY PROCESS

Assembly steps used for the construction of the sensor are listed below:

1. Using 400 grit sandpaper, sand each disk's inner face and clean with alcohol.

2. Clean Swagelok™ threads and O-ring groove with alcohol.

3. Wrap Teflon® tape around the 1/4 inch Swagelok™ and thread into the body (will be used to hold the coupler housing).

4. Wrap Teflon® tape around the 1/8 inch Swagelok™ and thread into the other side of the body (will be used to evacuate the sensor if needed).

5. Sand and clean coupler housing edges.

6. Mark the long lead legs of the coupler in order to accurately control the lengths of the fiber legs (clear and green colored legs).

7. Insert the input and output leads through the 1/4 inch Swagelok™ and the coupler housing.

8. Thread the output lead from the pigtailed laser through the Sumitomo Splice Protector.

9. Prepare the coupler's input lead and the pigtailed laser diode output fiber for splicing. The laser diode used in this project is a pigtailed Sharp LT010 (Appendix A). The pigtailed optical fiber is the same type of fiber used in the coupler. A UDT 550 Optical Power Meter was used to monitor one of the long lead coupler fibers in order to maximize the optical alignment prior to splicing.

10. Slip the splice protector over the splice and use a protection heater to shrink the protector around the spliced fibers.

11. Utilizing marks on the long lead coupler fibers cleave back the leads until a total of 5.422 ± 0.005 m of optical fiber remain on both legs.

12. Proceed to locate the optimal optical path difference (OPD). The output of the coupler's output leg was measured with a UDT 255 Photodetector amplified by an

Ithaco 1211 Current Preamplifier. It was displayed on an oscilloscope where the characteristic fringe pattern was observed indicating that the sensor was interferometric i.e., the OPD was within the coherence length of the single mode laser diode.

13. Measure the optical output power of all three coupler legs.

14. Proceed to maximize the modulation depth of the interferometric signal by removing small lengths (1 - 2 mm) of fiber from one of the sensing legs. The greatest modulation depth (i.e., the ratio of the amplitude of the AC components to the DC amplitude of the interferometric output) will occur when the OPD between the two sensing legs is within the coherence length of the laser.

15. As the power reflecting back from one of the sensing legs was weaker than the other leg, a result of the coupler ratio being 46/54 and not 50/50, this leg was silvered in order to increase the amount of light being reflected from it's cleaved end. In this research an optical isolator was not employed. The silvering process used is discussed further in Appendix B.

16. Both the sensing legs are wound into flat coils, using the fiber winding apparatus discussed earlier. Each coil consists of 5.0 m of fiber. A rubber adhesive is used to glue the coils in place (see Appendix A).

17. Attach the spindle to the body disk then, using Stycast® 1266 epoxy (see Appendix A), epoxy one coil to the inner face of the body disk. Care must be taken to ensure that the epoxy does not spread into the inner region around the spindle. In order to determine the effects of added mass and stiffness from the epoxy use a precise and measured amount of the epoxy to adhere the coil to the disk. In this case 0.53 gm of epoxy was used to hold the coil in place.

18. Tackiwax is used to build a dam around the inner lip of the cap disk, as well as a plug at the center of the disk (where the spindle will seat against the disk), to keep the Stycast® 1266 epoxy from spreading into these regions.

19. The second coil is epoxied on to the cap disk, again using a known amount (0.62 gm) of epoxy.

20. The tackiwax is removed and the corresponding areas of the disk are thoroughly cleaned using cotton swabs and alcohol.

21. The excess fiber lengths are wound on the inside wall of the cylinder and tacked into place with rubber adhesive.

22. The coupler is inserted into the coupler housing and aligned within the 1/4 inch Swagelok™. Using Uralite® 3130, a fast curing elastomer, needing approximately 48 hours to cure at room temperature, the coupler is potted into the coupler housing.

23. The cap is carefully positioned onto the body cylinder ensuring that the O-ring is properly seated in its groove. Using a nut, machine screw, and metal washer, the cap is tightened onto the body cylinder effectively sealing the sensor be compressing the O-ring that is inserted between these two sections.

IV. MECHANICAL TESTING

A. RESONANCE FREQUENCY TEST RESULTS

1. Motivation

Since accelerometers are designed to work below their resonance frequency, it is first necessary to determine the resonance frequency of the clamped disk. The spindle and disks arrangement in this accelerometer has a resonance frequency below that of a system with no added spindle according to the results of Handelman and Cohen [Ref. 13]. This is based on the ratio of the spindle's radius to the disk's radius and the spindle's height to the disk's thickness. (Since the spindle is made of the same material as the accelerometer, the density ratio is not a normalizing factor).

2. Tap Test Measurements

The resonance frequencies of each disk, and the composite system, were measured by tapping the disks and recording the resulting free decay response with either a General Radio 1560-P42 Microphone or an Endevco Accelerometer on a Nicolet 3091 Digital Storage Oscilloscope. A block diagram of the apparatus is shown in Figure 4.1. The free decay period was determined by measuring the elapsed time between a counted number of cycles. Several different

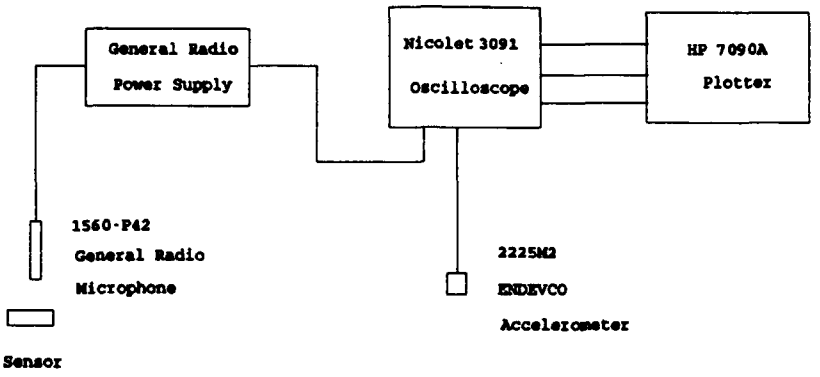

Figure 4.1 Block diagram of the free decay experiment apparatus.

techniques were used to attach the cap disk to the body in order to investigate how the resonance frequency changed for various boundary conditions.

One might expect that the measured values of the resonance frequency of the spindle-disk composite taken with the Endevco Model 2225M2 Accelerometer will be lower than the values obtained with the non-contacting microphone, since the accelerometer adds appreciably more mass than stiffness to the clamped system. The addition of the Endevco accelerometer to the spindle-disk composite increased the value of t′ from 0.35" to 0.88" (an increase of 151%) resulting in an increase of γ. At the same time the radius ratio, α, was not changed from its value of 0.22. As the stiffness of the composite system was not changed but the mass was there should be a decrease in the resonance frequency.

The results are shown in Table 4.1. The theoretical frequencies were calculated using eqn. (2.18) and the

TABLE 4.1 SPINDLE AND DISKS COMPOSITE RESONANCE FREQUENCIES FOR VARIOUS COUPLING METHODS

DESCRIPTION	FREQUENCY (Hz) Cap	Body
A. Theoretical Values		
1. Ideally clamped disk No load ($\Lambda^2 = 10.216$)	4979 ± 179	5027 ± 136
2. Ideally simply supported disk. No load (Λ^2=4.964)	2418 ± 87	2442 ± 66
B. Measured with Microphone		
No Spindle:		
1. Disks attached by C-clamps (no O-ring)	4733 ± 6	4736 ± 5
2. Disks attached by C-clamps with O-ring	4741 ± 13	4769 ± 6
With Spindle:		
1. Disks attached by spindle (no C-clamps or O-ring)	2199 ± 13	2432 ± 4
2. Disks attached by spindle with O-ring (no C-clamps)	2207 ± 4	2328 ± 74
3. Disks attached by spindle and C-clamps (no O-ring)	2248 ± 7	2260 ± 15
4. Disks attached by spindle and C-clamps with O-ring	2277 ± 4	2342 ± 3
C. Measured with Accelerometer		
1. Disks attached by spindle (no O-ring or C-clamps)	1587 ± 33	1588 ± 24
2. Disks attached by spindle with O-ring (no C-clamps)	1502 ± 1	1627 ± 23
3. Disks attached by spindle and C-clamps (no O-ring)	1449 ± 2	1447 ± 1
4. Disks attached by spindle and C-clamps with O-ring	1446 ± 3	1449 ± 2

appropriate eigenvalue for the assumed boundary conditions (as discussed in Chapter II). It should be noted that the resonance frequency of the composite system's disks will probably be lower than anticipated from Table 4.1 results as the fiber coils and the epoxy used to bond them to the disk will have added mass to the disks, without appreciably increasing their stiffness since the modulus of the epoxy is smaller than that of aluminum.

As shown in Table 4.1, the results of this test confirms the theory that the addition of the spindle, to this accelerometer, lowered the resonance frequency below the unloaded system. Each of the various methods employed to couple the system lowered the resonance frequency. Sections 1 and 2 of part B are included to demonstrate the resonance frequency of the composite system with no additional mass (spindle) added. Appendix C contains the data recorded during the tap test that was used to create Table 4.1.

Utilizing the data in Appendix C, a linear least-squares regression analysis was performed by plotting the period squared of the measured free decay oscillations (for both the General Radio microphone and the Endevco accelerometer) against the mass added to the disks. By evaluating the slope and intercept of these graphs the effective stiffness due to the combination of the disk stiffness and the stiffness added by the spindle plus the effective (unloaded) mass of the composite system can be determined. The analysis results are

shown in Figure 4.2 and Figure 4.3 for the cap and body disks respectively. Plots of the period squared vs. the added mass for the cap and body disks are shown in Figures 4.4 a and b.

The relationship between resonance frequency and added mass is derived by modifying eqn. (2.19) as follows:

$$f_* = \frac{1}{2\pi}\sqrt{\frac{k_{eff}}{m_{eff} + m_{add}}} \quad . \tag{4.1}$$

Equation (4.1) is then used to determine the period squared which will allow both k_{eff} and m_{eff} to be calculated.

$$T^2 = \left(\frac{4\pi^2}{k_{eff}}\right)(m_{add}) + (4\pi^2)\left(\frac{m_{eff}}{k_{eff}}\right) \quad . \tag{4.2}$$

Using the slope-intercept relationship and eqn. (4.2) then

$$k_{eff} = \frac{4\pi^2}{slope} \tag{4.3a}$$

and

$$m_{eff} = \frac{intercept}{slope} \quad . \tag{4.3b}$$

From the regression analysis data shown in Figure 4.2 the effective stiffness and mass for the cap disk are 3.3 x 10^6 kg/sec^2 and 8.8 gm. For the body disk the effective stiffness is 3.4 x 10^6 kg/sec^2 and effective mass is 7.7 gm (see Figure 4.3 for data).

Regression Analysis - Linear model: Y = a+bX [Tap Test: Sensor Cap Disk]

Dependent variable: T^2 x 10^-9 (sec^2) Independent variable: Added Mass (g)

Parameter	Estimate	Standard Error	T Value	Prob. Level
Intercept	104.89	19.7385	5.31399	.00181
Slope	11.8968	0.930241	12.7889	.00001

Analysis of Variance

Source	Sum of Squares	Df	Mean Square	F-Ratio	Prob. Level
Model	122930.64	1	122930.64	163.6	.00001
Error	4509.6493	6	751.6082		
Total (Corr.)	127440.29	7			

Correlation Coefficient = 0.982147 R-squared = 96.46 percent
Stnd. Error of Est. = 27.4155

Figure 4.2 Linear least-square regression analysis for the cap disk. Both the General Radio microphone and Endevco accelerometer data (listed in Appendix C) was used in the analysis.

Regression Analysis - Linear model: Y = a+bX [Tap Test: Sensor Body Disk]

Dependent variable: T^2 x 10^-9 (sec^2) Independent variable: Added Mass (g)

Parameter	Estimate	Standard Error	T Value	Prob. Level
Intercept	89.5809	23.7688	3.76884	.00930
Slope	11.5749	1.12019	10.333	.00005

Analysis of Variance

Source	Sum of Squares	Df	Mean Square	F-Ratio	Prob. Level
Model	116367.66	1	116367.66	106.8	.00005
Error	6539.3039	6	1089.8840		
Total (Corr.)	122906.97	7			

Correlation Coefficient = 0.973034 R-squared = 94.68 percent
Stnd. Error of Est. = 33.0134

Figure 4.3 Linear least-square regression analysis for the body disk. Both the General Radio microphone and the Endevco accelerometer data (listed in Appendix C) was used in the analysis.

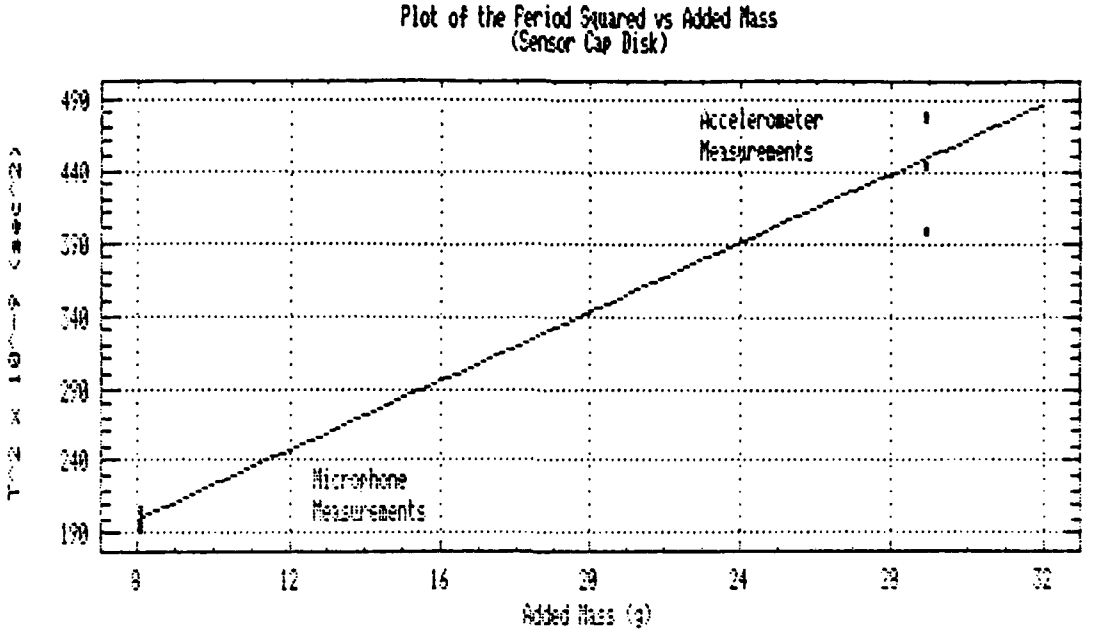

Figure 4.4a Plot of the period squared vs. the added mass for the cap disk.

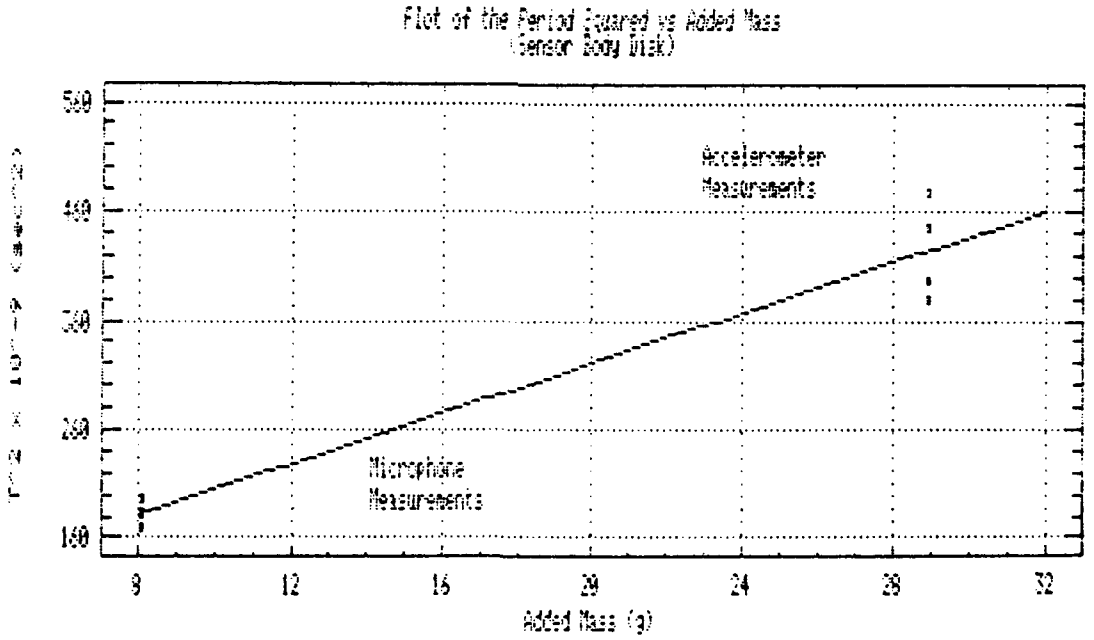

Figure 4.4b Plot of the period squared vs. the added mass for the body disk.

As a check against the effective mass of the sensor, determined above, it is possible to calculate the mass of the sensor by noting that

$$\rho = \frac{m}{At} \ , \tag{4.4}$$

and rearranging we arrive at

$$m = \rho A t = \rho \pi r^2 t \ , \tag{4.5}$$

where πr^2 is the area of the disk. Substitution of the appropriate values for the body disk results in the mass of the disk being m = 4.6 gm. As indicated in Chapter II, Section C, the effective mass for a mass loaded, double spring, harmonic oscillator is equivalent to the effective mass of a single, mass loaded, spring whose attached mass is half that of the double spring oscillator. Adding half the mass of the spindle (1.4 gm) to the mass of the body disk, determined from eqn. (4.5), results in the total effective mass of the sensor of m_{eff} = 6.0 gm. This is considerably less than the value for effective mass determined by the regression analysis of the tap test data. It should be noted that this test was conducted prior to the bonding of the optical fiber to the disks.

3. Comparison of the Results to the Handelman and Cohen Theory

As was expected from the theory presented by Handelman and Cohen, the resonance frequency of the composite accelerometer was below the resonance frequency, as determined theoretically and measured, for the unloaded case (Table 4.1). Determination of the cross-over value for the resonance frequency, based on the height ratio of the spindle and disk, allows for a practical method of ensuring that the resonance frequency (sensitivity) of a mass loaded accelerometer will be below (higher than) that of the unloaded sensor.

B. CALIBRATION TESTING

1. Instrumentation Set-up

Figure 4.5 shows the block diagram of the equipment that was used to calibrate the fiber-optic flexural disk accelerometer. The solid lines represent the piezoelectric accelerometer signal path and the dashed lines the optical accelerometer signal path. Due to the high sensitivity of the optical accelerometer, the power amplifier, used in the piezoelectric accelerometer test was not required. Figure 4.6 is a photograph of the piezoelectric and fiber-optic accelerometers on the shaker table.

a. Piezoelectric

In order to determine the sensitivity of the fiber-optic accelerometer a shaker table system was calibrated using

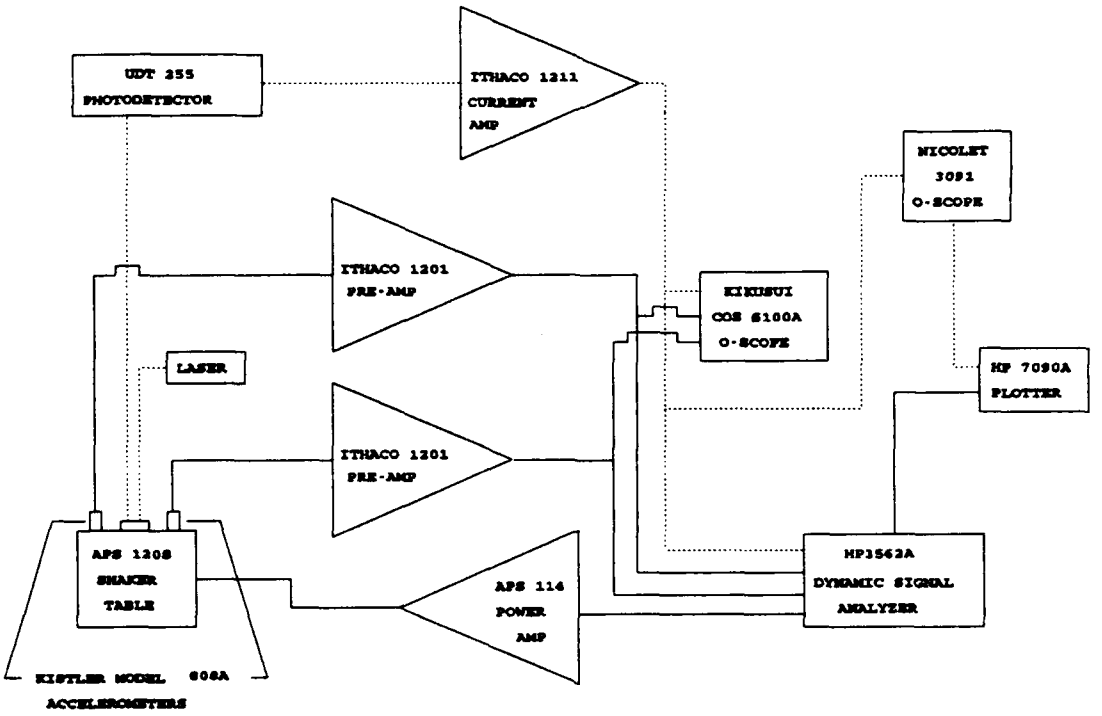

Figure 4.5 Block diagram of instrumentation for vibration calibration (solid lines) and optical testing (dashed lines).

piezoelectric (quartz) accelerometers. The instrumentation used is shown in Figure 4.5 and consisted of an Acoustic Power Systems Model 120S shaker table [Ref. 16], driven by a Hewlett Packard 3562A dynamic signal analyzer through an Acoustic Power Systems Model 114 power amplifier. Two Kistler Model 808A Quartz accelerometers (S/N 1785 and 1786) were attached at several locations around the shaker table to verify uniformity of the acceleration of the table surface. Both outputs were amplified by Ithaco 1201 pre-amplifiers and displayed on a Kikusui Model COS 6100A oscilloscope to compare

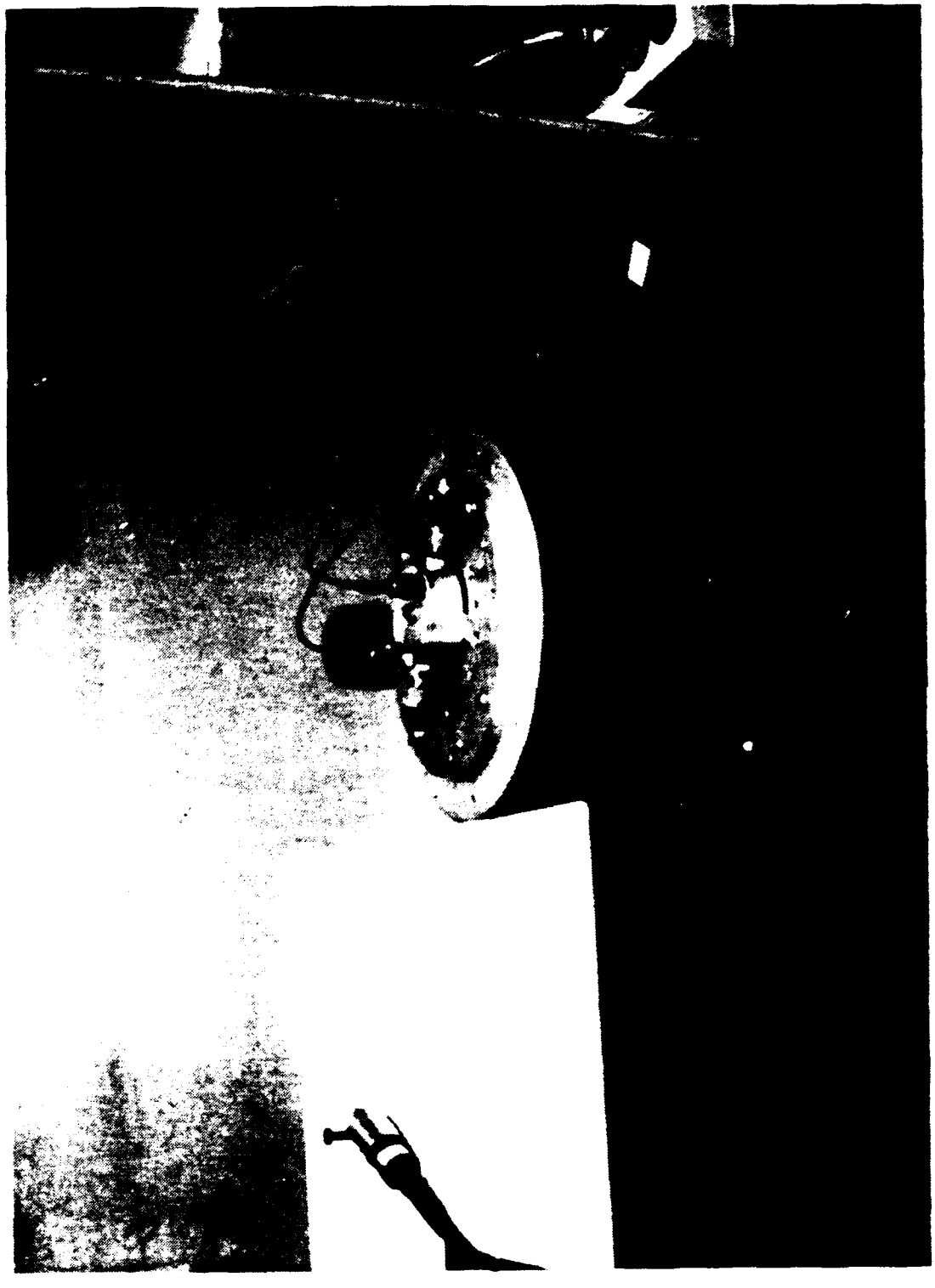

Figure 4.6 Fiber-optic and piezoelectric accelerometers mounted on the APS Shaker Table.

their amplitudes and phase. Additionally, the output from a Kistler accelerometer, S/N 1786, was taken from the pre-amplifier to the HP 3562A Dual Channel dynamic signal analyzer and used as the reference signal. The signal from the second Kistler accelerometer was returned to the dynamic signal analyzer as a test signal. A Hewlett Packard 7090A plotter was attached to the dynamic signal analyzer to provide a hard copy of the analyzer output.

A Brüel and Kjær Type 4294 Calibration Exciter (S/N 343643) was used to calibrate both Kistler accelerometers at 158.7 Hz. The accelerometers had sensitivities that were within 7.1% of each other. The accelerometers were also checked by applying an acceleration level of 9.8 $msec^{-2}$ peak to the shaker table (at this level a ball bearing placed on the table will just begin to shake and rattle). The sensitivities of the accelerometers determined in this manner were within 5.6% of each other.

During the acceleration test of the sensor the Kistler accelerometers demonstrated that the shaker table was not accelerating uniformly across its surface. Although the table accelerated evenly over its surface from 50 to approximately 1300 Hz, above this frequency the vibration levels had to be monitored carefully. In the region of uneven acceleration, the output from the Kistler accelerometers would be out-of-phase and display unequal amplitudes.

b. Optical

The optical instrumentation consisted of the fiber-optic flexural disk accelerometer and its attached laser source. The output of the accelerometer illuminated a UDT 255 photodetector followed by an Ithaco 1211 current amplifier and displayed on the Kikusui oscilloscope, the HP3562A and a Nicolet 3091 digital storage oscilloscope that was attached to the HP7090A plotter. The accelerometer was attached to the APS shaker table with a small amount of tackiwax. As mentioned earlier, the APS 114 power amplifier was not required when the sensor was tested on the shaker table.

2. Measurement Technique

The phase change produced in this fiber-optic Michelson interferometer, which is proportional to the change in acceleration, was measured by the method of fringe counting. The number of fringes (or light-dark cycles) in the interferometric signal per corresponding peak-to-peak change in the acceleration signal was counted. Shown in Figure 4.7 is an example of six fringes of phase modulation for a peak-to-peak acceleration cycle 7.3 m/sec^2.

A check on the accuracy of the fringe counting technique was done by the Bessel Zeroing Technique. Two frequencies (452 Hz and 1250 HZ) were used in this technique. The resulting acceleration sensitivity (4.31 $rad/msec^{-2}$ and 3.44 $rad/msec^{-2}$) lie between the values measured by the fringe

counting method at 400 Hz, 500 Hz, 1200 Hz, and 1275 Hz. Details of this calibration technique can be found in [Ref. 17 - 19].

3. Frequency Response Results and Analysis

The response of the accelerometer was measured in a surface normal mode i.e., the disks were normal to the direction of the shaker table excitation. The results of the testing are shown in Figure 4.8. This is a plot of acceleration sensitivity vs. the log of the frequency and indicates a maximum at approximately 2390 Hz.

The acceleration sensitivity is $\Delta\phi/a_c = 5.5 \pm 1.7$ radians/m sec^{-2} and it is independent of the frequency up through 1200 Hz. From 1200 Hz up to approximately 1900 Hz only a few data points were obtainable due to the shaker table response. Over the frequency range of 50 Hz to 2150 Hz the acceleration sensitivity is $\Delta\phi/a_c = 5.0 \pm 1.8$ radians/m sec^{-2}. Above this frequency the acceleration sensitivity increases to a maximum at 2450 Hz, which corresponds to the sensors resonance frequency.

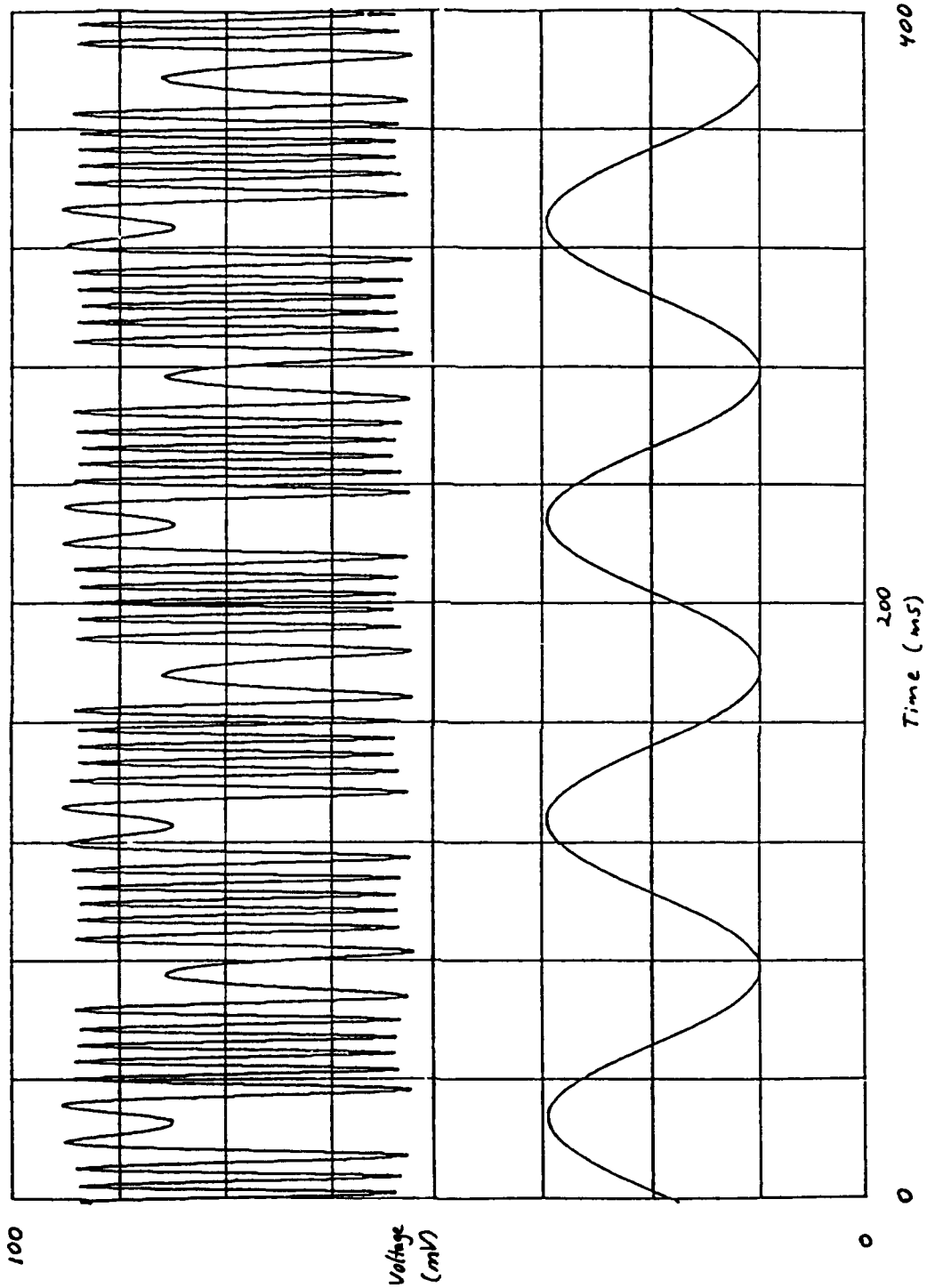

Figure 4.7 Piezoelectric accelerometer signal (lower trace) for 7.3 m/sec^2 peak-to-peak and the interferometric signal showing 6.0 fringes peak-to-peak excursion at a frequency of 1 kHz.

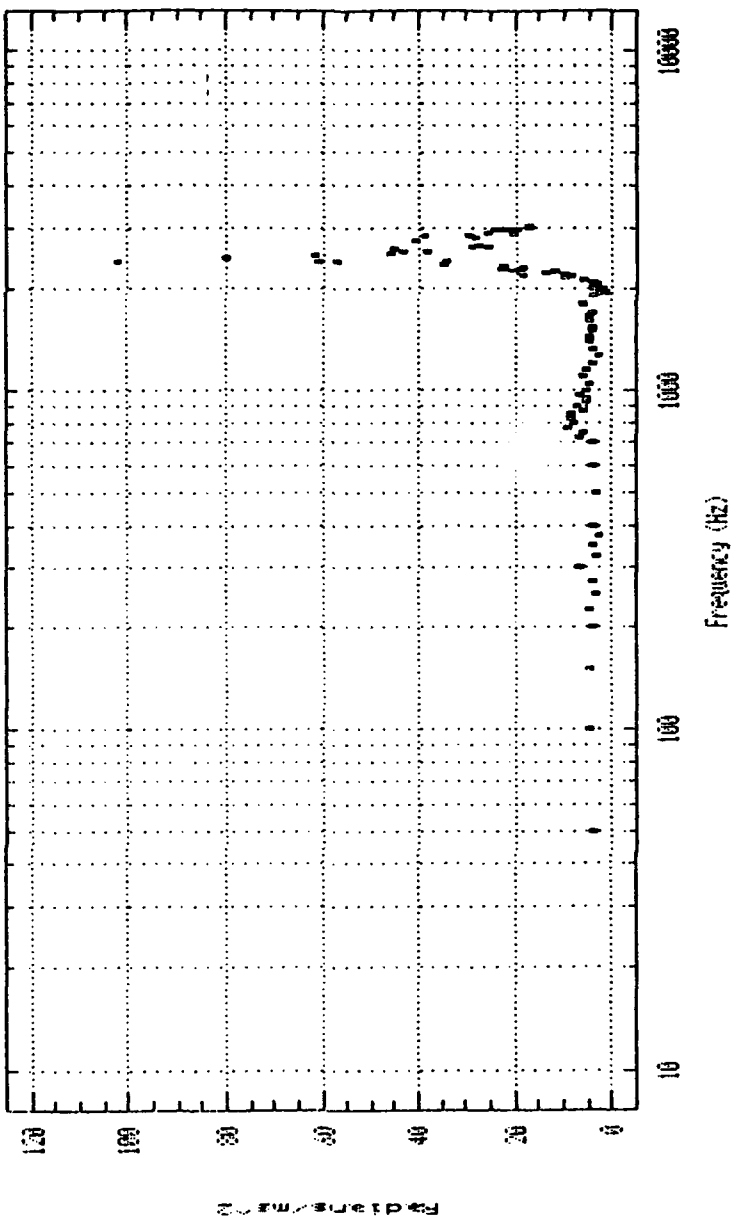

Figure 4.8 Acceleration sensitivity as a function of frequency for this fiber-optic accelerometer.

V. CONCLUSIONS AND RECOMMENDATIONS

A. PERFORMANCE

1. Comparisons to other Fiber-Optic Accelerometers

Several different fiber-optic interferometric accelerometers have been constructed over the past twelve years. Table 5.1 is a listing of three accelerometers that have been reported in the literature including the one described in this thesis. Included in Table 5.1 is a comparison of the normalized force sensitivity ($\Delta\phi/\phi ma_c$). The normalized force sensitivity or fractional phase change per unit of force is determined by dividing the phase change ($\Delta\phi$) by the product of the total radian length of fiber (ϕ), the mass, m, and acceleration, (a_c):

$$\frac{\Delta\phi}{\phi\Delta F} = \frac{\Delta\phi}{\phi m a_c} \quad . \tag{5.1}$$

A wave length of 830 x 10^{-9} m and an index of refraction of 1.5 was used in the calculations of ϕ. The fiber-optic accelerometer discussed in this thesis lies between the NPS mandril sensor [Ref. 20] and the LITTON [Ref. 21] accelerometers in terms of the fractional phase change per unit force. The total variation in normalized force sensitivity among the three designs is only a factor-of-three.[Ref. 22] The Table also includes comparisons

of mass, fiber length, resonance frequency, and the sensitivity, resonance frequency squared product.

TABLE 5.1 COMPARISON OF THREE FIBER-OPTIC ACCELEROMETERS [Ref. 22]

Parameter	Style NPS [Ref. 20]	LITTON [Ref. 21]	FLEX. DISK
Acceleration Sensitivity, M_c (radians/g)	10000	630	49
Moving Mass, m (kg)	0.575	~0.025	0.008
Fiber Length, L (m) (one leg)	7.4	37.5	5
Resonance Frequency, f_o (Hz)	240	1300	2450
Normalized Sensitivity $\Delta\phi/\phi ma_c$ (1/N)	10.6×10^{-6}	3.0×10^{-6}	5.5×10^{-6}
Accel. Sens. times (Res. Freq.)^2, Mf_o^2 (1/m)	5.9×10^{7}	10.9×10^{7}	3.1×10^{7}

2. Summary

This first generation fiber-optic flexural disk accelerometer demonstrates a "push-pull", Michelson configured interferometer. The sensing legs and spindle are internally attached within the sensor body. The internal placement of the sensing legs allows this sensor design to be used in a variety of acceleration environments that might be hazardous

to the optical fiber or the epoxy bonding the fiber to the disks.

B. DESIGN AND OTHER EQUATIONS REVISITED

Utilizing the values for effective mass and stiffness determined by the regression analysis of the tap test data, the predicted resonance frequency, eqn. (2.24), of the accelerometer is 3.1 kHz for the cap disk and 3.3 kHz for the body disk. Both of these values are higher than all the observed values listed for the various sealing methods, that included the spindle, in Table 4.1.

The values obtained from the tap test do not include the mass that was added due to the bonding of the optical fiber to the disks. The mass added by the epoxy is 1.2 gm, which increases the effective mass of the accelerometer, as determined by eqn. (4.5), to 5.8 gm. Using the resonance frequency of the sensor and eqn. (2.19), the effective stiffness of the sensor is 1.4×10^6 kg/sec^2. This is lower than the cap and body disks k_{eff} determined by the regression analysis. If the added mass of the spindle is included (2.7 gm) the effective stiffness becomes 2.0×10^6 kg/sec^2.

These differences between the values reinforces the difficulty in separating the complex relationship between added mass, effective mass, and effective stiffness. The best predictor of the resonance frequency remains the Handelman and

Cohen theory for determining whether the frequency will be above or below the unloaded sensors resonance frequency.

C. RECOMMENDATIONS

This first generation Michelson configured fiber-optic flexural disk accelerometer has demonstrated performance over broad frequency range. Changes to the material and techniques used to fabricate the sensor should be investigated [Ref. 23]. Changing the end disks to a more flexible material will allow for higher sensitivity. An increase in sensitivity would also be obtained if the sensor were to incorporate four coils of fiber verses two as was illustrated in Figure 2.4c. Consideration would have to given to protecting the outer coils from potential damage, if this optical wiring scheme was used.

Additional flexural disk geometries should be investigated. A variation of the flexural disk accelerometer discussed in this thesis which uses disks (plates) which are supported at their center and mass loaded at their perimeters as shown in Figure 4.9 and proposed in [Ref. 24].

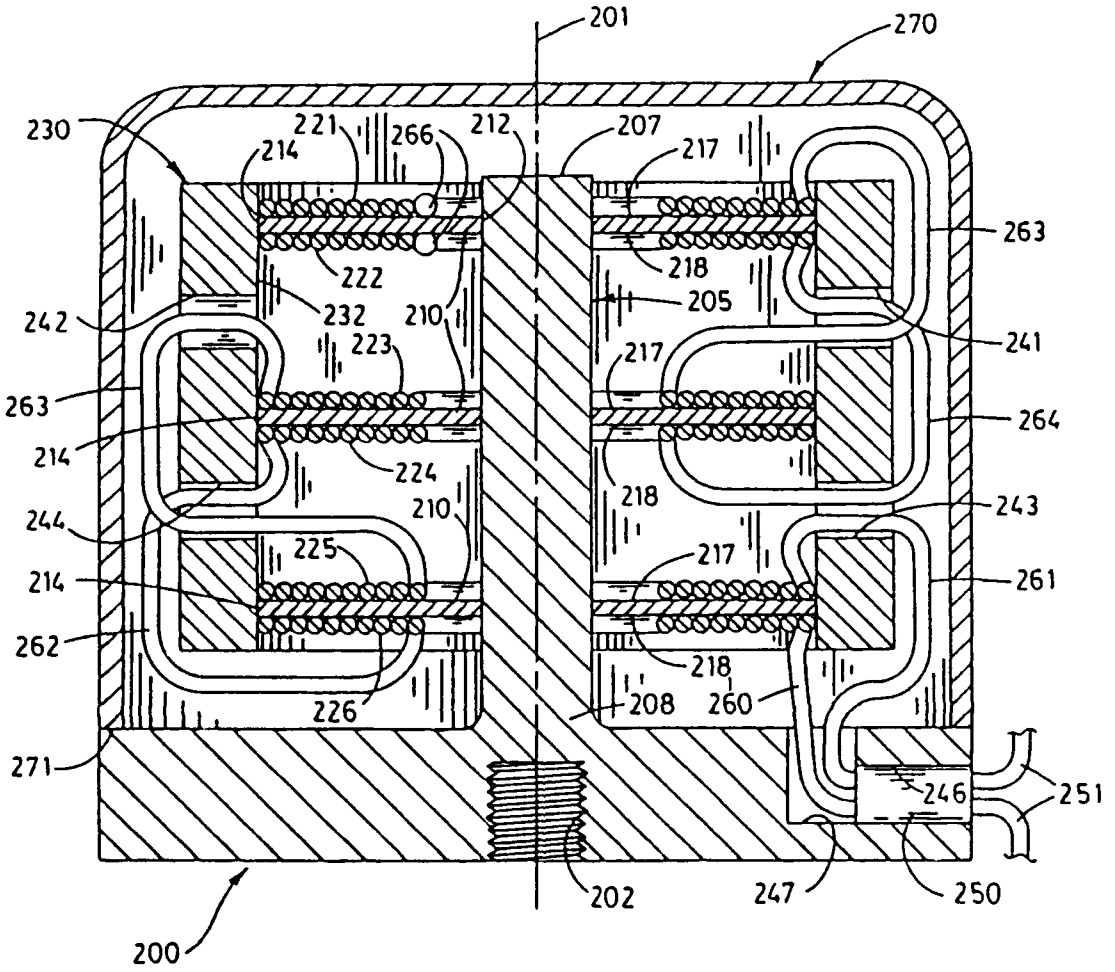

Figure 5.1 Variation of the flexural disk accelerometer [After Brown, Hofler, and Garrett, Ref. 24].

APPENDIX A

COMPONENTS OF THE OPTICAL SYSTEM

CORNING Telecommunications Products Division
Corning Glass Works
Corning, New York 14831, USA
Tel 607-974-4411
Telex 932498

Corguide Optical Fiber

Product Information

Flexcor-850™ Single-Mode Fiber

Issued 1/87

1.0 Introduction

An increasing number of specialized communication and sensor applications are making use of the advantages offered by single-mode fiber operating in the 780-850 nm wavelength region.

Much of the original work in fiber optic communications systems involved operation at or around 850 nm. This experience has produced a wide variety of components suitable for operation in this window, including some of the highest speed opto-electronic devices currently available. One of the most promising recent developments is the 780 nm laser used in compact disc players. These devices are extremely inexpensive, and 780 nm operation fits readily into the capability of the short-wavelength single-mode fiber described here.

Sensor Applications

One advantage of this fiber is the increased sensor sensitivity it allows in many applications. In these applications, sensitivity increases with decreasing wavelength. Therefore, 850 nm operation offers a significant increase in sensitivity over 1300 nm fiber. Although there is an attenuation increase involved in moving from 1300 nm to 850 nm, the typical lengths involved in these systems preclude the need for the extremely low attenuation found in the 1300 and 1550 nm windows of single-mode fiber.

Another advantage is the enhanced resistance to bending induced attenuation increases compared to 1300 nm single-mode fibers. As a result, this fiber can be tightly coiled, as it might be in a fiber sensor coil, without a significant increase in attenuation.

This bending loss resistance allows Corning to offer this product in two different diameters, 80 µm and 125 µm. The telecommunications industry has settled on 125 µm as the standard cladding diameter, and this means there are a wide variety of connectors and other components available for this fiber size. There are two advantages offered by 80 µm fiber, however. First, for a given coil diameter, an 80 µm fiber will be under significantly lower stress than a 125 µm fiber would be. This is especially important on small coils such as those found in fiber optic rotation sensors (gyroscopes). In addition, volume can be a major consideration in some sensor applications. The smaller fiber diameter allows the coating diameter to be decreased as well, yielding the smallest possible package.

Communications Applications

In addition to the benefits 850 nm single-mode fiber offers for sensors, it also has advantages that can be utilized in communication and datacom applications as well. The high bandwidth and low attenuation inherent in single-mode fiber allows this fiber to outperform most 850 nm multimode products in these areas. Although the zero dispersion wavelength for this fiber is in the 1300 nm region, it offers bandwidth values of greater than 5 GHz·km.

A variety of high bandwidth applications, both digital and analog, have proven the capabilities of this fiber. Work is currently in progress by a number of organizations to adapt the low cost 780 nm laser, used in compact disc players, for optical communications use. When this becomes practical, 850 nm single-mode fiber could become the fiber of choice for many LAN applications.

2.0 Product Design

Corning's Flexcor-850™ single-mode fiber is a matched clad, step-index, high delta design optimized for operation at 850 nm. The core is germania doped silica, surrounded by a pure silica cladding. The fiber contains no phosphorus, and the water (OH^-) content is typically less than 10 parts per billion.

The fiber is manufactured by the Outside Vapor Deposition (OVD) process. This results in low water content, excellent geometry control, and low, uniform attenuation. The three spectral attenuation plots shown below demonstrate the excellent bending performance of this product. Figure 1 shows the fiber attenuation when measured on a large diameter (14") measurement reel under no tension. Figure 2 shows the same fiber on a smaller (6") shipping reel under approximately 25 g tension. Figure 3 shows the attenuation for the same fiber with 100 m wrapped on a 1" diameter mandrel under minimal tension. Although attenuation has increased somewhat at longer wavelengths, attenuation is unaffected at the operating window.

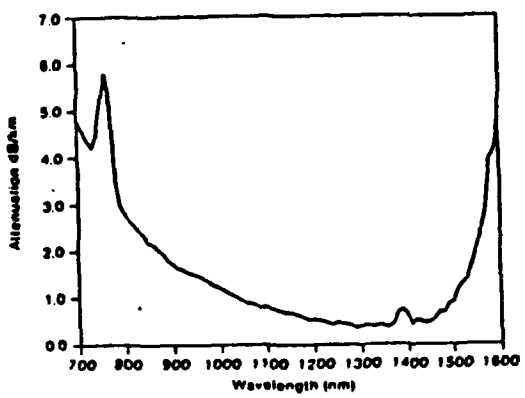

Measurement Reel Attenuation

Figure 1

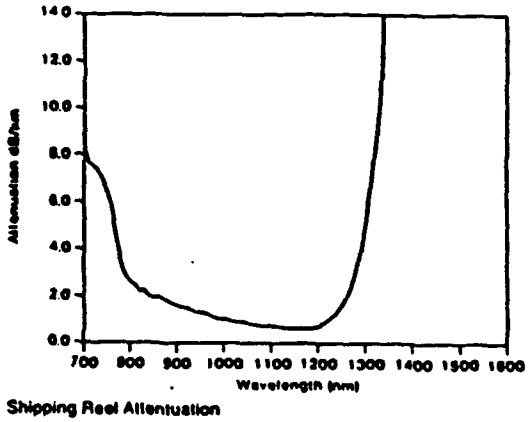

Shipping Reel Attentuation

Figure 2

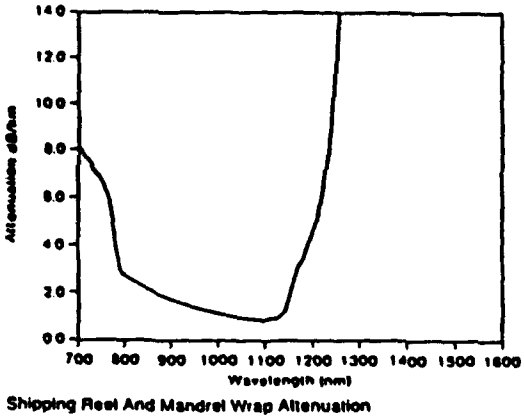

Shipping Reel And Mandrel Wrap Attenuation

Figure 3

The coatings used for this product are Corning CPC3 and CSB3, the same coatings applied to Corning's telecommunication fibers. These are UV curved acrylate coatings that provide excellent protection from microbending induced attenuation. In addition, these coatings are stable over the fiber's operating range of −60°C to +85°C, keeping temperature induced attenuation increases to a minimum.

The specifications shown in the following section reflect the performance guaranteed by Corning for this product. Every fiber shipped meets or exceeds these specifications.

3.0 Flexcor-850™ Fiber Specifications

3.1 *Optical Parameters*

3.1.1 Attenuation at 850 nm	≤ 3.0 dB/km ≤ 2.3 dB/km
3.1.2 Cut-Off Wavelength	750 ± 50

3.2 *Physical Parameters*

Nominal Delta (Equivalent Step Index)	0.45
Cladding Diameter	125 ± 2 µm 80 ± 2 µm
Coating Diameter	185 ± 15 µm' 250 ± 15 µm 500 ± 25 µm
Clad Ovality	≥ 0.98
Core/Clad Concentricity	≤ 1 µm
Standard Lengths	1.1 km-12.6 km
Minimum Order ($100.00 Cutting Charge for Non-Standard Lengths)	100 meters
Proof Stress	0.35 GN/m² (50 kpsi) 0.70 GN/m² (100 kpsi) 1.40 GN/m² (200 kpsi)

'80 µm fiber only

For more information about Corning's Flexcor-850™ single-mode fiber, contact the Advanced Fiber Products Department, Corning Glass Works, MP-RO-03, Corning, NY 14831 or call (607) 974-4144.

Developmental Optical Fiber Warranty

This warranty relates to optical fibers which are currently undergoing development and testing. Corning represents that each reel of these fibers sold by it meets applicable test [illegible] mechanical strength, light attenuation and bandwidth. Corning makes no warranty, however, as to the results to be obtained from the use of these fibers. Moreover, Corning reserves the right to change these fibers and/or their manufacturing or measurement techniques in the future. If any of these fibers fail to satisfy this warranty, Corning's sole obligation will be to provide replacement fibers. In no event shall Corning be responsible for removal or installation costs or other incidental or consequential damages. THE FOREGOING WARRANTY IS IN LIEU OF ALL OTHER WARRANTIES EXPRESS OR IMPLIED INCLUDING THE WARRANTIES OF MERCHANTABILITY AND FITNESS FOR A PARTICULAR PURPOSE.

AMPHENOL PRODUCTS
FIBER OPTIC PRODUCTS

INTERFUSE 945 SERIES Single Mode Coupler
Typical Fabrication Data

Model Number : 945-999-1327 10m Output Leads

Serial Number: 14553

Wavelength :		820 nm
Coupling Ratio :		50 +/- 10%
Excess Loss :		<1.0 dB
Op. Temp. Range :		-55 to +125 C
Temp. Depend	-CR:	<0.1 dB
	-EL:	<0.1 dB
Polar Depend :		<0.05 dB
Uniformity :		<0.1 dB
Directivity :		>-55 dB

Measured Coupling Ratio: 54 %

Measured Excess Loss: .13 dB

QA Approved [illegible]

Date 2/22/99

Lead Identification System

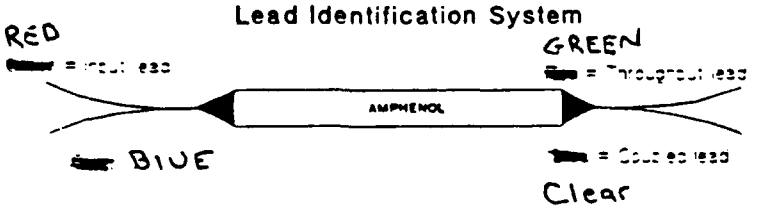

LT010MC/MD/MF

Features
- Wavelength, 810nm
- Single transverse mode

Application
- Medical apparatus
- Short-distance communications
- Light source for optical information processing

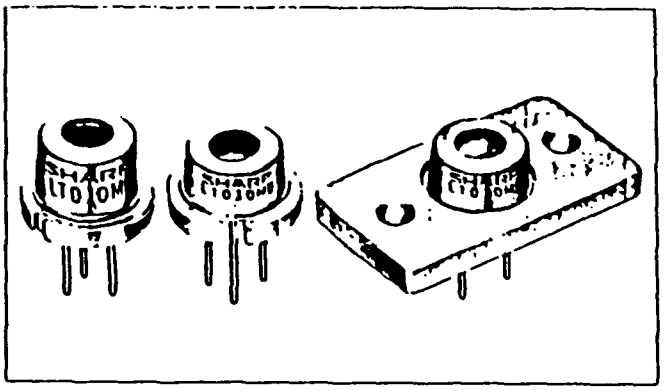

Absolute Maximum Ratings

(Tc = 25°C)

Parameter		Symbol	Ratings	Units
Optical power output		Po	5	mW
Reverse voltage	Laser	V_R	2	V
	PIN		30	
Operating temperature *1		Topr	−10 ~ +60	°C
Storage temperature *1		Tstg	−40 ~ +85	°C
Soldering temperature *2		Tsol	260 (less than 5 seconds)	°C

*1 Case temperature *2 At point 1.6 mm from lead base

Electro-Optical Characteristics *1

(Tc = 25°C)

Parameter		Symbol	Condition	Ratings MIN.	Ratings TYP.	Ratings MAX.	Units
Threshold current		Ith	—	—	50	80	mA
Operating current		I_{op}	Po = 3mW	—	65	100	mA
Operating voltage		Vop	Po = 3mW	—	1.75	2.2	V
Wavelength *2		λp	Po = 3mW	800	810	820	nm
Monitor current		Im	Po = 3mW, V_R = 1.5V	0.2	0.9	2.0	mA
Radiation Angle *3	Parallel to junction	θ //	Po = 3mW	8	11	16	deg
	Perpendicular to junction	θ ⊥	Po = 3mW	20	33	45	deg
Emission point accuracy	Angle	Δθ //	Po = 3mW	—	—	±2	deg
		Δθ ⊥	Po = 3mW	—	—	±3	deg
	Position *4	Δx, Δy, Δz	—	—	—	±80	μm

*1 Initial value *3 Angle at 50% peak intensity (full width at half maximum)
*2 Single transverse mode *4 Not specified for LT010MF

Electrical Characteristics of Photodiode

(Tc = 25°C)

Parameter	Symbol	Condition	Ratings MIN.	Ratings TYP.	Ratings MAX.	Units
Sensitivity	S	V_R = 1.5V	—	0.3	—	mA/mW
Dark current	I_D	V_R = 1.5V	—	—	150	nA
Terminal capacitance	Ct	V_R = 1.5V	—	8	20	pF

Fig. 125 Forward Current vs. Forward Voltage

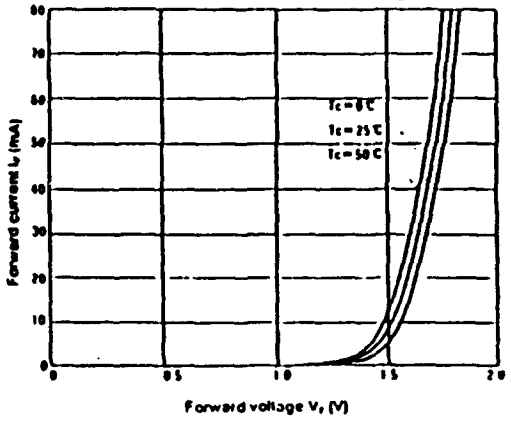

Fig. 126 Optical Power Output vs. Forward Current and Monitor Current

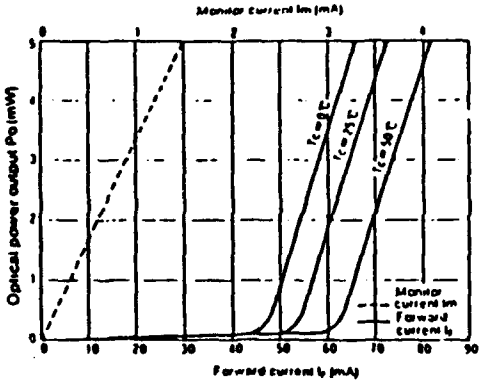

Fig. 127 Threshold Current vs. Temperature

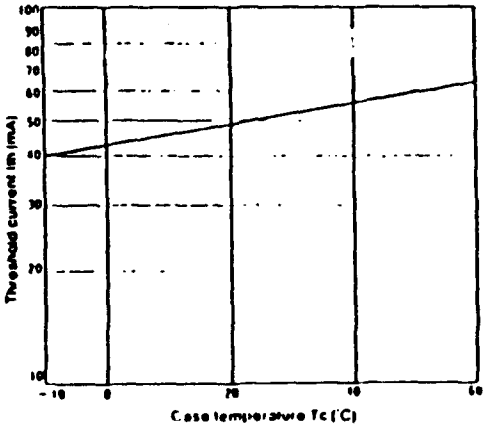

Fig. 128 Wavelength vs. Temperature

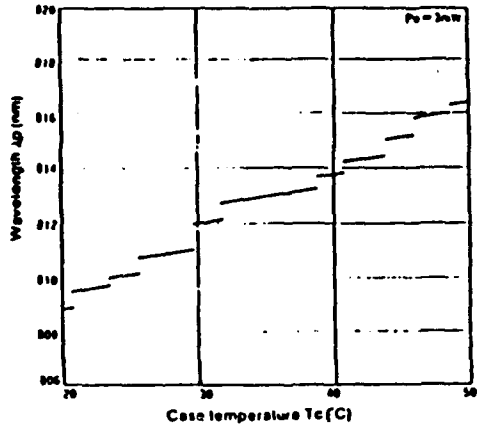

Fig. 129 Optical Power Output Dependence of Wavelength

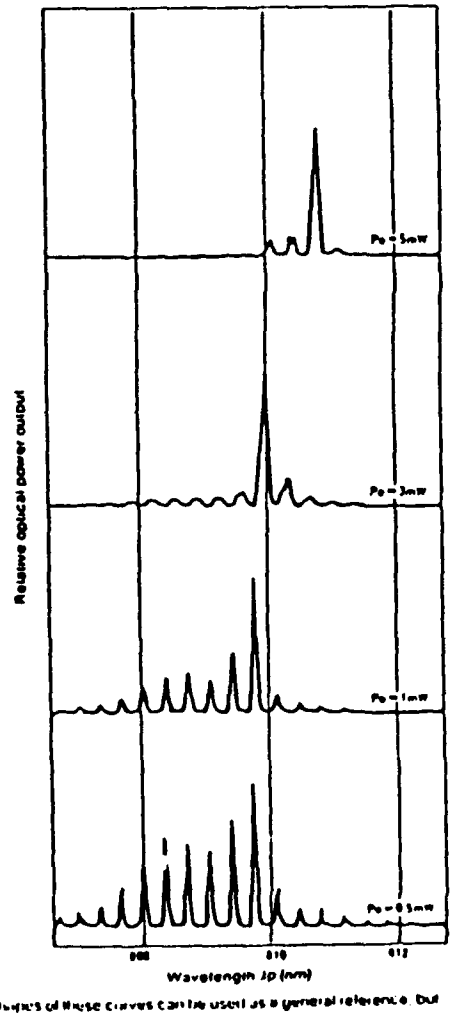

Note All data on this page is typical only and is not guaranteed as a specification. The shapes of these curves can be used as a general reference. But the actual characteristics will vary from device to device.

SEASTAR OPTICS
A DIVISION OF SEASTAR INSTRUMENTS (1978) LTD.

CANADA Seastar Optics
P.O. Box 2430, 2045 Mills Rd., Sidney, B.C., Canada V8L 3S1
Telephone (604) 656-0891 Telex 049-7526

U.S.A. Seastar Optics
316 Second Avenue South Seattle, WA 98104 U.S.A.
Telephone (206) 623-2855 Telex 4937-056

LASER DIODE PIGTAIL TEST DATA

Model No. PT-300 **Date** Oct 21/87

Serial No. 0370 **Tested by** Duncan Powers

LIGHT - CURRENT CHARACTERISTICS

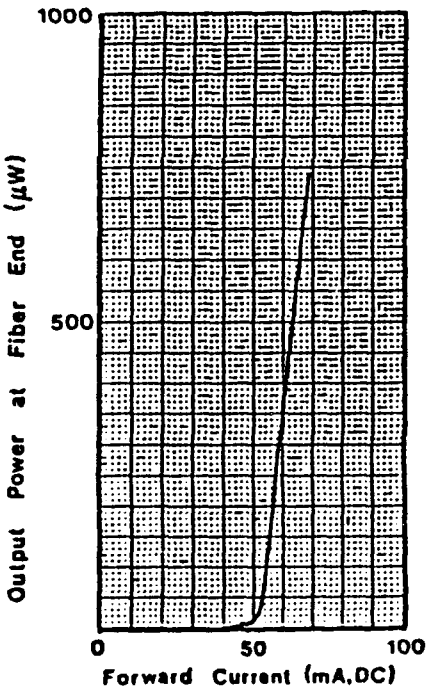

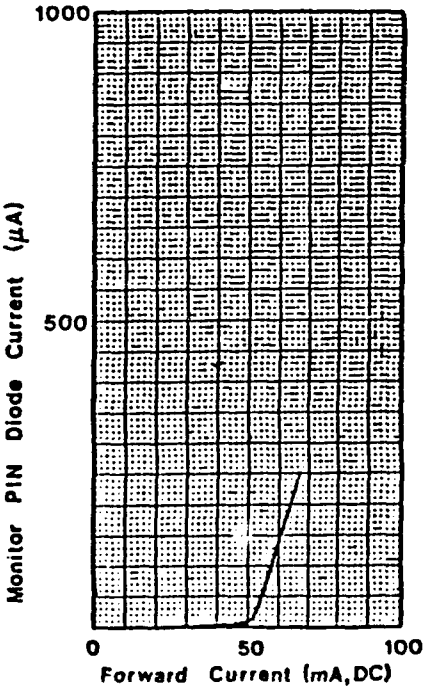

HEXCEL chemical products
RESIN CHEMICALS GROUP

URALITE® 3130

URETHANE CASTING ELASTOMER

80-85 Shore A

25-30 Shore D

TECHNICAL DATA BULLETIN

- No moisture sensitivity
- Excellent hydrolytic stability (Reversion Resistance)
- *No TDI, no 4,4'-Methylene-bis-(2-chloroaniline)*
- Fast cure, quick demolding
- High abrasion resistance
- Low Viscosity
- *Good Electrical Properties*
- Good Adhesion to many substrates

DESCRIPTION.

Uralite 3130 is a two component, natural amber or black urethane casting elastomer. This tough room temperature mixing and curing system has excellent handling characteristics. Uralite 3130 is a middle of the hardness range, general purpose, versatile Uralite elastomer. It does not exhibit typical moisture sensitive characteristics of most urethane elastomers.

USES:

- Electrical and Electronic Encapsulating
- Molds and Mold Facings
- Metal forming pads
- Flexible snakes
- Gaskets
- Abrasion resistant parts

PROPERTIES:

	Test Method	Value	(Metrics)
Shore Hardness A/D	ASTM D 2240-68	80-85/25-30	
Viscosity Part A – cps	ASTM D 2393-71	3400	
Viscosity Part B – cps	ASTM D 2393-71	120	
Mixed Viscosity – cps	ASTM D 2393-71	2000	
Tensile Strength – psi (kg/cm²)	ASTM D 412-68	2750	(193)
Elongation – %	ASTM D 412-68	250	
Tear Strength – pli (kg/cm)	ASTM D 624 Die C	250	(45)
Dielectric Strength – step @ 77°F (25°C), volts/mil	ASTM D 149-64	240	
Dielectric Constant – @77°F (25°C)	ASTM D 150-54T		
10^6 Hz		5.6	
10^3 Hz		7.2	
Volume Resistivity – @77°F (25°C) @1000V, ohm-cm	ASTM D 257-70	1×10^{13}	
Surface Resistivity – @77°F (25°C) 1000V, ohms	ASTM D 257-70	2×10^{13}	

PROPERTIES: (Continued)

	Test Method	Value	(Metrics)
Insulation Resistance – @77°F (25°C) ohms after 28 days @ 95°F (35°C) 95% RH	WE ATS612	1×10^{11}	
Pot Life – min. @ 77°F (25°C)	ASTM D 2471-71	14	
Shrinkage - in/in (mm/mm)	ASTM D 2566-69	0.0016	
Density	ASTM D 792-66		
Cured Compound lbs/in³ (g/cm³)		0.039	(1.07)
Part A lbs./gal. (g/cm³)		8.58	(1.03)
Part B lbs./gal. (g/cm³)		9.15	(1.10)
Demolding Time – hrs @ 77°F (25°C)		4	
Demolding Time – hrs @ 175°F (79°C)		1	
Complete Cure – days @ 77°F (25°C)		2 - 4	
Complete Cure – hrs. @ 175°F (79°C)		2 - 3	
Color		Amber or Black	
Ratio (By Weight):			
Part A		100	
Part B		30	
Ratio (By Volume):			
Part A		100	
Part B		28	

These physical properties are representative of typical values obtained by tests conducted in the Chemical Products Division laboratory.

STORAGE:

Uralite 3130 should be stored in a cool dry area. Avoid temperatures above 90°F and below 65°F. Always blanket Uralite 3130 with dry nitorgen or 8440 Inert Blanketing Gas and reseal container after use.

SURFACE PREPARATION SUGGESTIONS:

Porous materials, such as plaster and wood, must have all surfaces that come in contact with Uralite 3130 well-sealed with a sealer which is compatible with urethane (acrylic sealers are suggested). After sufficient drying time, approximately thirty (30) minutes after last coat, the final surface preparation consists of the application of a release agent such as Partingkote® 8302 (wiping off excess) to accomplish a complete and uniform release coating.

MIXING:

Ratio: Parts by Weight Part A – 100 Part B – 30

Ratio: Parts by Volume Part A – 100 Part B – 28

Weigh both components into same container and stir slowly for 2-4 minutes, scraping the sides and bottom of container periodically to include unmixed material which may adhere to these surfaces. Care must be taken to avoid whipping air into mixture. Pour the thoroughly mixed Uralite 3130 onto the prepared surface and allow to cure. Working pot life of Uralite 3130 is approximately 14 minutes.

CURING:

Near ultimate physical properties are normally attained after 2 days at room temperature (77°F). Curing of Uralite 3130 may be accelerated by heating for 1-2 hours at 175°F. Demolding can be accomplished after 4 hours at room temperature.

PACKAGING:

UNIT DESIGNATION	PART A	PART B	UNIT NET WEIGHT
12 Qt. Pack (pre-weighed)	12-One Qt. Cans	12-½ Pint Cans	22 lbs. 13.12 ozs.
Pail Pack	5 Gal. Pail	2½ Gal. Can	52 lbs.
Drum Pack	55 Gal. Drum	30 Gal. Drum	585 lbs.

CAUTION:

FOR INDUSTRIAL USE ONLY.

This product contains an isocyanate based prepolymer, amines and heavy metal catalysts which are harmful if swallowed. It does not contain toluene diisocyanate or 4,4' methylene bis-(2-chloroaniline). It may cause burns or skin irritation. Use only in a well ventilated area. Protect skin and eyes from contact and avoid inhalation of vapors.

Should skin contact occur, wash with soap and water. For eye contact, flush with water immediately and obtain medical attention. If swallowed, drink water, induce vomiting and contact a physician immediately.

WARRANTY The following is made in lieu of all warranties, express or implied: Seller's only obligation shall be to replace such quantity of this product which has proven to not substantially comply with the data presented in the Manufacturer's latest bulletin describing the product. In the event of the discovery of a non-conforming product, Seller shall not be liable for any property loss or damage, direct or consequential, arising out of the use of or the inability to use the product. Before using user shall determine the suitability of the product for his intended use, and user assumes all risks and liability whatsoever in connection therewith. Statements relating to possible use of our product are not guarantees that such use is free of patent infringement or is approved by any government agency. The foregoing may not be changed except by an agreement signed by an officer of seller.

HEXCEL CORPORATION, RESIN CHEMICALS GROUP
20701 NORDHOFF STREET, CHATSWORTH, CALIFORNIA 91311 • (213) 882-3022

807

Printed in U.S

PLASTICS/CERAMICS FOR ELECTRONICS

Telephone TWX
Canton, Mass. 02021 (617) 828-3300 (710) 348-1324
Gardena, Calif. 90248 (213) 321-6650 (910) 346-6736
Northbrook, Ill. 60062 (312) 272-6700 (910) 686-0006

Emerson & Cuming, Inc.
DIELECTRIC MATERIALS DIVISION
CANTON, MASSACHUSETTS

TECHNICAL BULLETIN 7-2-26C

STYCAST® 1266

Transparent High Impact Room Temp. Cure Epoxy Casting Resin

STYCAST 1266 is a clear, low viscosity casting resin which when fully cured has outstanding toughness and impact strength. STYCAST 1266 can be cured at room temperature.

STYCAST 1266 has been used for display embedments. It has been used to bond lenses and sheets of glass for good visibility. STYCAST 1266 has good moisture resistance, electrical properties and adhesion to metal, glass and plastics. After catalyst addition, viscosity at room temperature is extremely low, making it easy to pour. Vacuum processing is not always needed. It will readily impregnate windings.

Long exposure of the cured resin to temperatures above 250°F (121°C) will cause some discoloration. Physical and electrical properties are not appreciably affected.

Typical Properties:

Mixed Viscosity at 77°F (25°C), cps	650
Specific Gravity	1.18
Hardness, Shore D	75
Izod Impact, ft. lbs. /in. (kg. cm. /cm.) of notch	2 (11)
Compressive Strength, psi (kg/cm^2)	10,000 (700)
Tensile Strength, psi (kg/cm^2)	6,000 (422)
Volume Resistivity, ohm-cm	6×10^{14}
Dielectric Strength, volts/mil (kv/mm)	400 (15.8)
Dielectric Constant, at 10^6 Hz	3
Dissipation Factor, at 10^6 Hz	0.02
Flexural Strength, psi (kg/cm^2)	20,000 (1,406)
Index of Refraction	1.56

Instructions for Use:

1. Prepare materials and mold for use.
2. Add 28 parts of Part B to 100 parts by weight of Part A. Mix thoroughly. Pot life will be about 1/2 hour. Use small batches. Use multiple pouring for castings over 100 grams.
3. Pour. Use vacuum evacuation if necessary.
4. Allow to stand at room temperature for 8 hours. The casting can be removed from mold when hard. A post cure at 200°F (93°C) for 2 hours will increase the hardness of the cured resin and its dielectric strength.
5. Curing at temperatures of 125°F to 150°F (51°C to 66°C) to speed production is possible, and depends both on resin mass, and the geometry of the unit to be potted. To determine optimum conditions, user should run a few experiments on his particular unit.

The handling of this product should present no problems if ordinary care is exercised to avoid breathing vapors, if the skin is protected against contamination, if swallowing is avoided, and if the eyes are protected. We recommend observing the precautions in Public Health Service Publication No. 1040, May 1963, which is available from the Superintendent of Documents, U. S. Government Printing Office, Washington D. C. 20402.

The shelf life of this product is 6 months when stored in sealed, unopened containers at temperatures no higher than

This information, while believed to be completely reliable, is not to be taken as warranty for which we assume legal responsibility nor as permission or recommendation to practice any patented invention without license. It is offered for consideration, investigation, and verification.

APPENDIX B

SILVERING OF CLEAVED FIBER ENDS

Because the reflection of light from one fiber leg was weaker than the other leg, it was necessary to coat the cleaved end of the weaker leg with silver to increase the amount of light that was reflected. The increased reflected light increases the power from the output fiber and the amount of light that is returned to the laser diode. The increased light at the laser may necessitate the insertion of an optical isolator to minimize the effect of the increased noise.

The process used in this research to silver the fiber end is called the Rochelle Salts process [Ref. 25]. This was one of three processes initially reviewed that could be utilized to produce a reflective coating for the fiber end [Ref. 25 - 26]. Since two of the proposed processes involved the chemical reaction between Silver Nitrate ($AgNO_3$) and ethanol, which could result in an explosion, they were not considered suitable for this project.

The Rochelle Salts process requires that two solutions be combined in order to initiate the chemical reaction in which silver particles will precipitate out of solution. Solution A is made by dissolving 5 gm of Silver Nitrate ($AgNO_3$) in 300 ml of distilled water (H_2O). Dilute Ammonium Hydroxide (NH_4OH) is added until the resulting precipitate (caused by the

initial addition of NH_4OH) is almost redissolved. This solution is than filtered and distilled water is added to make 500 ml of solution.

Solution B is made by dissolving 1 gm of $AgNO_3$ in a small quantity of distilled water, and 0.83 gm of Rochelle Salts in another small quantity of distilled water. Both of these solutions are added to 500 ml of boiling (distilled) H_2O. The combined solutions are then boiled for 30 more minutes. The solution then filtered while hot, and distilled H_2O is added to make 500 ml.

The two solutions, A and B, can be stored up to two months if sealed and kept in a dark environment. Over time, the solutions will lose their potency and will fail to react with any consistency. During this project several batches of solution were made and it was noted that the longest that a batch was useful for use in this application was approximately three weeks. When a project required that silvering be done a fresh set of solutions was formulated.

It is not necessary to make the total amount of each solution, the "recipe" can be reduced to suit the need. In addition, both solutions should be disposed of in a environmentally safe manner consistent with their constituents.

APPENDIX C

TAP TEST DATA

The values listed are averaged from the five tests run conducted on each of the four different combinations or methods used to make the composite system. Included are the two values for the composite system with no added mass.

CAP DISK
Measured by the General Radio Microphone

Description	Cycles	Time (ms)	Freq (kHz)	Period x 10^{-9} (sec^2)	Added Mass (g)
Disks held by C-clamps (no O-ring)	37	7.82	4.733	44.64	0
Disks held by C-clamps with O-ring	37	7.81	4.740	44.5	0
Disks held by spindle (no C-Clamps, no O-ring)	33.6	15.3	2.197	207.18	8.06
Disks held by spindle, C-clamps (no O-ring)	42.8	19.04	2.248	197.88	8.06
Disks held by spindle, O-ring (no C-clamps)	14.4	6.53	2.206	205.41	8.06
Disks held by spindle, C-clamps, O-ring	17.0	7.47	2.277	192.85	8.06

CAP DISK
Measured by the Endevco Accelerometer

Description	Cycles	Time (ms)	Freq (kHz)	Period x 10^{-9} (sec^2)	Added Mass (g)
Disks held by spindle (no C-Clamps, no O-ring)	28.6	18.04	1.587	396.95	28.90
Disks held by spindle, C-clamps (no O-ring)	56.4	38.93	1.449	476.54	28.90
Disks held by spindle, O-ring (no C-clamps)	28.2	18.77	2.205	442.98	28.90
Disks held by spindle, C-clamps, O-ring	27.2	18.82	1.446	478.54	28.90

BODY DISK
Measured by the General Radio Microphone

Description	Cycles	Time (ms)	Freq (kHz)	Period x 10^{-9} (sec^2)	Added Mass (g)
Disks held by C-clamps (no O-ring)	37	7.81	4.736	44.58	0
Disks held by C-clamps with O-ring	37	7.76	4.769	43.97	0
Disks held by spindle (no C-Clamps, no O-ring)	47.2	19.41	2.432	169.13	8.06
Disks held by spindle, C-clamps (no O-ring)	38.6	17.08	2.260	195.79	8.06
Disks held by spindle, O-ring (no C-clamps)	17.4	7.48	2.382	184.52	8.06
Disks held by spindle, C-clamps, O-ring	18.0	7.69	2.342	182.27	8.06

BODY DISK
Measured by the Endevco Accelerometer

Description	Cycles	Time (ms)	Freq (kHz)	Period x 10^{-9} (sec^2)	Added Mass (g)
Disks held by spindle (no C-Clamps, no O-ring)	11.2	7.05	1.588	396.55	28.90
Disks held by spindle, C-clamps (no O-ring)	27.4	18.93	1.447	477.46	28.90
Disks held by spindle, O-ring (no C-clamps)	30.6	18.82	1.627	377.77	28.90
Disks held by spindle, C-clamps, O-ring	28.2	18.81	1.499	444.76	28.90

LIST OF REFERENCES

1. D. A. Brown, "A Fiber-Optic Flexural Disk Hydrophone", Master's Thesis in Engineering Acoustics, Naval Postgraduate School, (March 1989), DTIC Report № AD-B132 243; D. A. Brown, T. Hofler, and S. L. Garrett, "High Sensitivity, Fiber-Optic, Flexural Disk Hydrophone with Reduced Acceleration Response", Fiber and Integrated Optics, **8**(3), pp. 169-191, (1989).

2. J. A. Flayharty and B. M. Fitzgerald, "Design and Fabrication of Fiber Optic Acceleration Canceling Hydrophone", Master's Thesis in Engineering Acoustics and Master's Thesis in Applied Science, (June 1989 and September 1989).

3. D. L. Gardner, "A Fiber-Optic Interferometric Seismic Sensor with Hydrophone Applications", Ph. D. Dissertation in Engineering Acoustics, Naval Postgraduate School, (September 1987), DTIC Report № AD-B-112-487.

4. Busurin, V. I., Semenov, A. S., and Udalov, N. P., "Optical and Fiber Optic Sensors (Review)", Sov. Journal of Quantum Electron., **15** (5), pp. 595-621, May 1985.

5. Giallorenzi, T. A., Bucaro, J. A., Dandridge, A., Sigel, Jr., G. H., Cole, J. H., Rashleigh, S. C., and Priest, R. G., "Optical Fiber Sensor Technology", IEEE J. Quantum Electrontics, **18**, pg. 626, 1982.

6. Lyamshev, L. M. and Smirnov, Yu. Yu., "Fiber Optic Acoustic Sensors (Review)", Sov. Phys. Acoust. **29** (3) pp. 169-180, May-June 1983.

7. Jackson, D. A., "Monomode Optical Fibre Interferometers for Precision Measurement", J. Phys. E: Sci. Instrum. Vol. 18, 1985.

8. D. Halliday and R. Resnick, Fundamentals of Physics, pp. 734, Second Edition, (John Wiley & Sons, New York, 1981).

9. G. B. Hocker, "Fiber-optic Sensing of Pressure and Temperature", Appl. Opt., **18**, pp. 1445-1448, (1979).

10. D. A. Brown, "Optical Fiber Interferometric Acoustic Sensors Using Ellipsoidal Shell Transducers", Ph. D. Dissertation in Engineering Acoustics, Naval Postgraduate School, (June 1991).

11. L. Kinsler, A. Frey, A. B. Coppens and J. V. Sanders, Fundamentals of Acoustics, 3rd ed., pp. 2-3, 94, 462, (John Wiley & Sons, New York, 1982).

12. A. W. Leissa, Vibration of Plates, NASA Tech Doc: Sp-160-N70-18461, (1969), Washington, D.C..

13. G. Handelman and H. Cohen, "On the Effects of the Addition of Mass to Vibrating Systems", ASTIA Document No. 96045, (September 1956).

14. Interfuse 945 Series Single Mode Coupler, Amphenol Corporation, Wallingford, CT.

15. Telecommunications Products Division, Corning Glass Works, Corning, NY, (Corguide Optical Fiber, Flexcore-850™ Single-Mode Fiber).

16. Acoustic Power Systems, Carlsbad, CA, (Model 120S Shaker Table).

17. J. A. Bucaro, N. Lagakos, J. H. Cole, and T. G. Giallorenzi, "Fiber Optic Acoustic Transduction", in Physical Acoustics XVI, W. P. Mason and R. N. Thurston, editors, pp. 385-455, (Academic Press, 1982).

18. G. B. Mills, S. L. Garrett, and E. F. Carome, "Fiber Optic Gradient Hydrophone", Fiber Optic and Laser Sensors II, Proc. Soc. Photo-Optical Inst. Eng. (SPIE), **478**, pp. 98-103, (1984).

19. E. F. Carome and M. P. Satysur, "Fiber Optic Acoustic Sensors", in Fiber Optics, B. Bendow and S. S. Mitra, editors, pp. 658-659, (Plenum Press, New York, 1979).

20. D. L. Gardner and S. L. Garrett, "Fiber Optic Seismic Sensor", in Fiber Optic and Laser Sensors V, Proc. Soc. Photo-Optical Inst. Eng. (SPIE), **838**, pp. 271-278, (1987).

21. M. R. Layton, B. A. Danver, J. D. Lastofka, and D. P. Bevan, "A Practical Fiber Optic Accelerometer", in Fiber Optic and Laser Sensors V, Proc. Soc. Photo-Optical Inst. Eng. (SPIE), **838**, pp. 279-284, (1987).

22. D. A. Brown and S. L. Garrett, "An Interferometric Fiber Optic Accelerometer", in Fiber Optic and Laser Sensors VIII, Proc. Soc. Photo-Optical Inst. Eng. (SPIE), **1367**, pp. 282-288, (1990).

23. S. L. Garrett, D. A. Brown, B. Beaton, K. Wetterskog, and J. Serocki, "A General Purpose Fiber-optic Hydrophone Made of Castable Epoxy", in Fiber Optic and Laser Sensors VIII, Proc. Soc, Photo-Optical Instr. Eng. (SPIE), **1369**, pp. 13-29, (1990).

24. "Fiber optic flexural disk accelerometer", D. A. Brown, T. Hofler, and S. L. Garrett, Patent application, Navy Case 73054, (1991).

25. D. C. Miller, Laboratory Physics, 2nd ed., pp. 269, (Athenaeum Press, Boston, 1932).

26. S. Kupiec, Department of Physics, University of Alabama, personal communications.

INITIAL DISTRIBUTION LIST

		No. Copies
1.	Physics Department ATTN: Dr. D. A. Brown Code PH Naval Postgraduate School Monterey, CA 93943	4
2.	Physics Department ATTN: Dr. S. L. Garrett Code PH/Gx Naval Postgraduate School Monterey, CA 93943	4
3.	Physics Department ATTN: Dr. D. L. Gardner Code PH/Gd Naval Postgraduate School Monterey, CA 93943	1
4.	Library, Code 52 Naval Postgraduate School Monterey, CA 93943-5002	2
5.	Defense Technical Information Center Cameron Station Alexandria, VA 22304-6145	2
6.	Commanding Officer Naval Sea Systems Command ATTN: Mr. G. Kamalakis - Code 06UR4 Mr. C. Jacobson - Code 06KR22 Washington, D. C. 20362-5102	2